Politecnico di Torino

POLITECNICO DI TORINO

Department of Mechanical and Aerospace Engineering

Master's degree course in Aerospace Engineering

Master's Degree Thesis

Low-speed camera for high frequency dynamic behavior characterization with DIC

Academic tutor:

Prof. Daniele Botto

Supervisor:

Eng. Davide Mastrodicasa

Candidate:

Gian Paolo Sellitto

288777

April 2023

Abstract

In the aerospace, automotive, and other mechanical industries, it is crucial to assess the structure's dynamic behavior in order to validate the products. Traditional methods of performing vibration measurement and Experimental Modal Analysis (EMA), such as using accelerometers, can provide accurate measurements but are invasive and may not be able to comprehensively measure the dynamic response of the test structure, as they can provide information only at discrete points.
An alternative approach for performing EMA is to use camera-based methods, such as Digital Image Correlation (DIC), which can provide full-field displacement and strain measurements without physical contact with the object being studied.
However, this method is limited by the frame rate of the cameras, which is lower with respect to contact transducers. In this framework, high-speed cameras may initially seem like a more suitable solution for reaching higher frequencies, but they can result in lower resolution and higher testing costs due to the expense of acquiring such cameras.
Therefore, this thesis proposes two alternative methods for using DIC with low-speed cameras with the aim of characterizing the dynamics of structures at frequencies higher than the Nyquist-Shannon limit. The first method involves a random sampling scheme in time, which is coupled with a nonlinear optimization problem that seeks to reconstruct the initial randomly sampled signal with higher resolution. The second exploits the periodicity of the structure's dynamics excited by a shaker to under-sample the specimen over numerous excitation cycles and then remap the time history that characterizes the analyzed object.
The proposed approaches are validated through numerical validation and experimental tests on a cantilever beam. The results demonstrate the effectiveness of the proposed method of capturing the mode shapes of the structure at a frequency over the Nyquist-Shannon limit, focusing attention on the benefits and drawbacks of the proposed approach.

Acknowledgements

Arrivato alla fine di questo percorso universitario ci tengo a ringraziare le persone che mi hanno accompagnato in questo periodo ricco di emozioni, difficoltà ma soprattutto di grandi soddisfazioni.

In primis desidero ringraziare il mio relatore, il Professor Botto, per la sua disponibilità e per i suoi consigli sinceri. Ringrazio il mio supervisore, l'Ing. Davide Mastrodicasa, per avermi guidato durante il tirocinio, per le conoscenze trasmesse e per essere sempre stato disponibile ad ascoltare ogni mio dubbio. Grazie anche a tutte le persone che ho conosciuto a Lovanio con le quali ho condiviso una bellissima esperienza.

Ai miei genitori, per il loro supporto incondizionato e per tutto ciò che quotidianamente hanno fatto e continuano a fare per me. A mia sorella Simona, per essere stata una maestra di vita. A tutta la mia numerosa famiglia che mi ha sempre sostenuto nonostante la distanza.

Ad Andrea, Ciccio e Giuseppe, per essere stati la mia famiglia a Torino. A tutte le persone con le quali ho vissuto tante avventure in questa meravigliosa città. A Lorenzo, Emanuele, Gianmario e tutti i compagni con i quali ho condiviso i banchi del Politecnico. Agli amici di Avellino, rimasti vicino nonostante la distanza. Ai ragazzi del Polito Sailing Team con i quali ho partecipato ad una delle esperienze più formative di questi anni universitari. A Maria, Pasquale e Daniele, per avermi accolto con affetto nella loro famiglia.

Un ultimo ringraziamento, ma non per questo meno importante, lo devo a Giorgia, il mio amore, per aver sempre creduto in me e per avermi supportato, ma soprattutto sopportato, nei momenti più difficili.

Table of Contents

List of Tables

List of Figures

Acronyms

CS Compressive Sensing

DFT Discrete Fourier Transform

DIC Digital Imagine Correlation

EMA Experimental Modal Analysis

ESPI Electronic Speckle Pattern Interferometry

FRAC Frequency Response Assurance Criterion

FRF Frequency Response Function

IRF Impulse Response Function

LDV Laser Doppler Vibrometry

SDOF Single Degree Of Freedom

MDOF Multiple Degree Of Freedom

MIMO Multiple Input Multiple Output

MSE Mean Square Error

ROI Region Of Interest

SSD Sum Squared Difference

SNR Signal-to-Noise Ratio

TRAC Time Response Assurance Criterion

ZNSSD Zero Normalized Sum Squared Difference

Introduction

By estimating the modal parameter, EMA makes possible to evaluate a structure's dynamical characteristics. Usually, it is based on point-wise sensors connected to the structure, such as accelerometers, which due to their high resolution allow to reach high frequencies and permit a comparatively simple set-up. However, they can provide only local measurement, they have the drawback of adding mass to the system, which could affect the dynamic behavior of a virgin specimen, and they are exposed to wiring and electrical noise introduction.

Figure 1: Ground Vibration Test on an Aircraft with contact transducers

As an alternative, non-contact methods, that are increasingly employed in these days, can relay on different technologies like Laser Doppler Vibrometry (LDV), Electronic Speckle Pattern Interferometry (ESPI) or Digital Imagine Correlation (DIC) [1, 2, 3]. These methods can provide spatially dense information for modal analysis without using an overwhelming number of sensors and without mass loading effect, especially with the increasing use of lightweight structures [4].

In comparison to other non-contact technologies, DIC consists of a simple optical set-up that only required one or more cameras and a well enlightened speckled specimen, which is another reason why it is more frequently used in aerospace and automotive components, as well as rotating structures like turbine blades or helicopter rotors [5, 6]. However, the use of EMA based on DIC is limited by the frequency range that can be analyzed due to the sampling rate of the cameras, which is typically around 1000 fps (frames per second) for high-speed cameras, whereas the typical range of a piezoelectric accelerometer is 1 Hz to 10000 Hz [7]. Furthermore, the use of high-speed cameras may lead to reduced resolution and increased costs compared to low-speed cameras, which may still be desirable despite having a substantially lower sampling rate. Sampling rate capacity has a fundamental role because of aliasing, which is an error that occurs when two different sine waves have the same value at the sampling points. According to the Nyquist-Shannon's theorem, this error is known to occur when the sampling rate is less than the double the sampled signal frequency. In order to achieve both high resolution and the ability to detect high-frequency behavior of structures, various techniques such as under-sampling and remapping of time histories have been explored for measuring above the Nyquist frequency of the camera [8, 9, 10, 11].

Figure 2: Ground Vibration Test on an Aircraft with DIC

Scope of this work

For the previously mentioned reason, the aim of this thesis is to investigate and test some methodologies for performing DIC analysis using low-speed cameras that can characterize the dynamics of the component under study at frequencies exceeding the Nyquist-Shannon theorem's upper limit. In this work, two techniques are examined. These are referred to as *Random Sampling* and *Smart Aliasing* in the chapters that follow.

The application of the *Random Sampling* method to EMA was carried out specifically in the case of impact excitation. The method involves acquiring with a random scheme samples of the displacement of the specimen using cameras and processing the data through DIC. The ultimate goal is to recover the modal response through a nonlinear optimization method. In the field of Compressive Sensing (CS) different methodologies based on a random sampling scheme were investigated [12, 13]. They proved the feasibility of using random sampling with an average sampling frequency lower than the Nyquist-Shannon limit, as a correct acquisition method to then recover the structure's modal response. On this statement is based a recent work that uses a time domain random sampling acquisition scheme and a subsequent modal sparse recovering for the case of impact excitation [10]. The *Random Sampling* method that is presented in this thesis uses the same optimization process.

On the other hand, the *Smart Aliasing* method is limited in its application for EMA, as it can only be used when the analyzed specimen is excited with a periodic excitation. The method relies on sampling at a fixed rate that is lower than the Nyquist-Shannon limit. Nevertheless, it is possible to reconstruct the excitation cycle at a sampling frequency greater than the Nyquist-Shannon limit by repeating the excitation for a specified number of cycles using an appropriate sampling scheme that will be described in this work. Another study that investigated the same method and that was taken as example is [11].

In this study, the aforementioned methods are described and validated from both a numerical and experimental standpoint. The research was conducted during an internship at Siemens Digital Industry offices in Leuven, and the experimental procedure was carried out in the laboratory located there.

The organization of this thesis is as follows:

- **Part I** presents the theoretical background necessary as a basis for the concepts explained in the rest of the work.
- **Part II** describes the Random Sampling method, along with the numerical and experimental validation.
- **Part III** describes the Smart Aliasing method and presents both the numerical and experimental validation, including related analyses.

Part I

Theoretical Background

Chapter 1

Modal Analysis

The objective of this chapter is to provide a brief introduction to the theoretical basis of modal analysis, which is a technique used to determine the natural dynamic characteristics of a system [14, 15]. Modal analysis can be performed through two approaches: *Analytical* and *Experimental Modal Analysis*, both of which are important in the study of system dynamics.

The first one is based on the prior knowledge of the structure geometry, the boundary conditions and the material properties (mass, stiffness and damping). This information is sufficient to derive the system's modal parameters, which include natural frequencies, damping factors, and mode shapes. These parameters are able to fully describe the dynamic behaviour of the structure. The analytical approach is typically used in the design phase of a system, where the structural parameters are known and can be used to predict the system's response to external excitations.

The second relies on measurements of dynamic input forces and output responses on the structure. These measurements can be translated into Frequency Response Function (FRF), which represents the ratio between output and input as a function of frequency. These FRFs can be expressed as a function of the modal parameters that characterize the structure's dynamic properties.

In modal analysis, some basic assumptions are typically made:

- *Linearity*: The system's behaviour is assumed to be linear, which means that its dynamics can be described by a set of linear, second-order differential equations, and it is based on the superposition principle.

- *Time invariance*: The system's dynamic characteristics are assumed not to change over time, as the differential equation coefficients are constant.

- *Observability*: All the necessary data have to be measurable, which means that it is possible to measure the response of the system to external excitation and that the response is sufficient to identify the modal parameters of the system.

- The *Maxwell's reciprocity principle* is most frequently assumed to govern the structure, if an input at a point p generates an output at q, the same input at q will generate the same output at p. This results in mass, stiffness, damping and frequency response function matrices that are symmetric.

To introduce fundamental concepts, an analysis of a single degree of freedom system (SDOF) is conducted, followed by an extension with the analysis of multiple degree of freedom systems (MDOF).

1.1 Single degree of freedom system (SDOF)

1.1.1 System equation, transfer function

When considering a viscously damped single degree of freedom system (as shown in Figure 1.1), the equation of equilibrium among all forces can be expressed as follows:

$$m\ddot{x}(t) + c\dot{x}(t) + kx(t) = f(t) \tag{1.1}$$

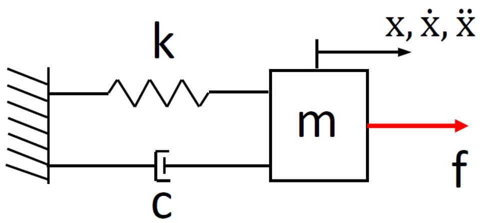

Figure 1.1: Single degree of freedom system

where:

- m: mass
- c: damping
- k: stifness
- x,$\dot{x}$,$\ddot{x}$: displacement, velocity, acceleration
- f: external force
- t: time

Assuming the initial displacement and velocity equal to zero in the Laplace domain (variable p), the equation can be written as:

$$(mp^2 + cp + k)X(p) = F(p) \tag{1.2}$$

or

$$Z(p)X(p) = F(p) \tag{1.3}$$

where Z is the *dynamic stiffness*.

It is possible to rewrite Equation 1.3 by defining the *transfer function* as $H(p) = Z^{-1}(p)$:

$$X(p) = F(p)H(p) \tag{1.4}$$

and express $H(p)$ in function of the system properties:

$$H(p) = \frac{1/m}{p^2 + (c/m)p + (k/m)} \tag{1.5}$$

where the denominator of this equation is the *system characteristic equation*. Evaluating the roots of this equation the *system poles* can be obtained as:

$$\lambda_{1,2} = -(c/(2m)) \pm \sqrt{(c/(2m))^2 - (k/m)} \tag{1.6}$$

Several parameters can be defined based on this equation:

The *undamped natural frequency* Ω_1 (rad/s), that corresponds to the root of a system without damping, obtained from Equation 1.6 when c=0:

$$\Omega_1 = \sqrt{k/m} \tag{1.7}$$

The *critical damping* C_c, which is that value the makes the term under the square root in Equation 1.6 equal to zero:

$$C_c = 2m\sqrt{k/m} \tag{1.8}$$

The *damping ratio* ζ_1 defined as the ratio between the damping and the critical damping C_c:

$$\zeta_1 = C/C_c \tag{1.9}$$

The solution of the homogeneous system equation in the time domain, which physically corresponds to the solution of the system without external force, is:

$$x(t) = x_1 e^{\lambda_1 t} + x_2 e^{\lambda_2 t} \tag{1.10}$$

and depending on the value of the damping ratio ζ_1 the system will be:

- *Overdamped* ($\zeta_1 > 1$), the roots are real and negative, the system response is characterized by a decay only.
- *Critically damped* ($\zeta_1 = 1$), the roots are real, negative, and coincident, resulting in a system response that exhibits only exponential decay, occurring in the shortest possible time.
- *Underdamped* ($\zeta_1 > 1$), the roots are complex conjugate, the system response takes the form of a decaying oscillation.

Since in real-word systems damping ratio ζ_1 is less than ten percent (0.1), only the last scenario is taken into consideration. Consequently, solving Equation 1.6 results in:

$$\lambda_1 = \sigma_1 + j\omega_1 \qquad \lambda_1^* = \sigma_1 - j\omega_1 \tag{1.11}$$

where σ_1 is the *damping factor* and ω_1 is the *damped natural frequency.*
From these equations, other useful relations can be obtained, such as the one between the *damping factor* and the *damping ratio*:

$$\sigma_1 = -\zeta_1 \Omega_1 \tag{1.12}$$

Rewriting Equation 1.5 as a function of the system poles (Equation 1.11), the transfer function results:

$$H(p) = \frac{1/m}{(p - \lambda_1)(p - \lambda_1^*)} \tag{1.13}$$

and applying the theory of the partial fraction expansion, it can be rewritten as:

$$H(p) = \frac{A_1}{(p - \lambda_1)} + \frac{A_1^*}{(p - \lambda_1^*)} \tag{1.14}$$

where $A_1 = \frac{1/m}{j2\omega_1}$ and A_1,A_1^* are the so-called *residues.*

1.1.2 Frequency response function (FRF), Impulse response function (IRF)

The *transfer function*, as depicted in Equation 1.4, represents the relationship between the input X and the output F of the system, and can be expressed in both the frequency and time domains. By evaluating Equation 1.14 along the frequency axis ($j\omega$), the *frequency response function (FRF)* can be obtained:

$$H(p)|_{p=j\omega} = H(\omega) = \frac{A_1}{(j\omega - \lambda_1)} + \frac{A_1^*}{(j\omega - \lambda_1^*)} \tag{1.15}$$

While, evaluating the inverse Laplace transform of eq.1.14, the *impulse response function (IRF)* can be derived:

$$h(t_s) = A_1 e^{\lambda_1 t_s} + A_1^* e^{\lambda_1^* t_s} = e^{\sigma_1 t_s}(A_1 e^{j\omega_1 t_s} + A_1^* e^{-j\omega_1 t_s}) \tag{1.16}$$

1.2 Multiple degree of freedom system (MDOF)

In many instances, characterizing a system using only one degree of freedom is insufficient. Therefore, the concepts illustrated for a single degree of freedom system will be extended to a multiple degree of freedom system, introducing various significant parameters to conduct modal analysis.

1.2.1 System equation, transfer function

An example of a two degree of freedom system is depicted in Figure 1.2.

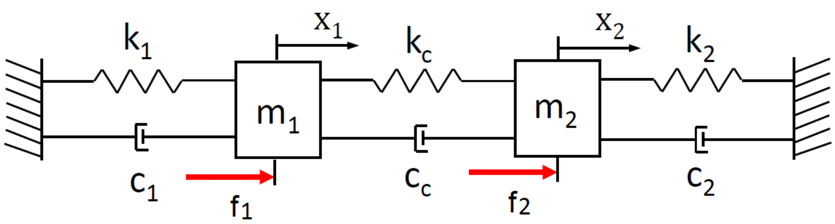

Figure 1.2: Two degree of freedom system

As in the preceding section, the analysis of the system commences with force equilibrium. In this particular scenario, the equations are related to each individual degree of freedom. Nonetheless, it is possible to obtain an equation similar to the SDOF equation by transforming the equations into a matrix form.
The equations of motion for the system are:

$$\begin{aligned} m_1\ddot{x}_1(t) + (c_1 + c_c)\dot{x}_1(t) - c_c\dot{x}_2(t) + (k_1 + k_c)x1(t) - k_cx_2(t) = f_1(t) \\ m_2\ddot{x}_2(t) + (c_c + c_2)\dot{x}_2(t) - c_c\dot{x}_1(t) + (k_c + k_2)x2(t) - k_cx_1(t) = f_2(t) \end{aligned} \tag{1.17}$$

in the matrix form, where (t) is deleted just for readability:

$$\begin{bmatrix} m_1 & 0 \\ 0 & m_2 \end{bmatrix} \begin{Bmatrix} \ddot{x}_1 \\ \ddot{x}_2 \end{Bmatrix} + \begin{bmatrix} c_1 + c_c & -c_c \\ -c_c & c_c + c_2 \end{bmatrix} \begin{Bmatrix} \dot{x}_1 \\ \dot{x}_2 \end{Bmatrix} + \begin{bmatrix} k_1 + k_c & -k_c \\ -k_c & k_c + k_2 \end{bmatrix} \begin{Bmatrix} x_1 \\ x_2 \end{Bmatrix} = \begin{Bmatrix} f_1 \\ f_2 \end{Bmatrix} \tag{1.18}$$

or:

$$[m]\{\ddot{x}\} + [c]\{\dot{x}\} + [k]\{x\} = \{f\} \tag{1.19}$$

where:

- $[m]$: mass matrix
- $[c]$: damping matrix
- $[k]$: stiffness matrix
- $\{x\}$: response vector as a function of time
- $\{f\}$: force vector as function of time

Equation 1.19 describes a general MDOF system, and its characteristics are contained within the matrices of mass, damping, and stiffness.
Similar to the methodology employed for a SDOF system, Equation 1.19 can be converted into the Laplace domain by assuming zero initial displacement and velocity:

$$(p^2[m] + p[c] + [k])\{X(p)\} = \{F(p)\} \tag{1.20}$$

Subsequently, the *dynamic stiffness matrix* $[Z(p)]$ and the *transfer function matrix* $[H(p)]$ can be defined by rewriting Equation 1.20 as:

$$[Z(p)]\{X(p)\} = \{F(p)\} \tag{1.21}$$

and as:

$$\{X(p)\} = [H(p)]\{F(p)\} \tag{1.22}$$

Where, using the fact that the inverse of a matrix can be evaluated from the adjoint matrix, the transfer function matrix can be expressed as:

$$[H(p)] = [Z(p)]^-1 = \frac{adj([Z(p)])}{|Z(p)|} \tag{1.23}$$

The denominator of Equation 1.23 corresponds to the system characteristic equation, and the roots of this equation, known as system poles, define the resonance frequencies of the system. To obtain these roots a general eigenvalue problem can be solved. By combining this identity:

$$(p[m] - p[m])\{X\} = 0 \tag{1.24}$$

with Equation 1.20, the following system of equations can be obtained:

$$(p[A] + [B])\{Y\} = \{F'\} \tag{1.25}$$

where:
$[A] = \begin{bmatrix} [0] & [m] \\ [m] & [c] \end{bmatrix}$, $[B] = \begin{bmatrix} -[m] & [0] \\ [0] & [k] \end{bmatrix}$, $\{Y\} = \begin{Bmatrix} p\{X\} \\ \{X\} \end{Bmatrix}$ and $\{F'\} = \begin{Bmatrix} \{0\} \\ \{F\} \end{Bmatrix}$.
When the forcing function is zero and the eigenvalue problem is solved using the equation:

$$|p[A] + [B]| = 0 \tag{1.26}$$

It is possible to demonstrate that the resulting eigenvalues are equivalent to the roots of the system's characteristic equation. Specifically, the eigenvalues will form 2N complex conjugate pairs, where N represents the number of degrees of freedom of the system.

$$[\Lambda] = \begin{Bmatrix} \lambda_1 & & & & & \\ & \ddots & & 0 & & \\ & & \lambda_N & & & \\ & & & \lambda_1^* & & \\ & 0 & & & \ddots & \\ & & & & & \lambda_N^* \end{Bmatrix} \tag{1.27}$$

where, just like for a SDOF, each root is characterized by the *damping factor* σ_r and the *damped natural frequency* ω_r that are respectively the real and the imaginary part.
Since λ_r, λ_r^* are roots of the *system characteristic equation* $|Z(p)|$ the *transfer function matrix* can be written from Equation 1.23 as:

$$[H(p)] = \frac{adj([Z(p)])}{\prod_{r=1}^{N} E(p - \lambda_r)(p - \lambda_r^*)} = \frac{adj([Z(p)])}{\prod_{r=1}^{2N} E(p - \lambda_r)} \tag{1.28}$$

where E is a constant. Applying the partial fraction expansion:

$$[H(p)] = \sum_{r=1}^{N} \left(\frac{[A]_r}{(p - \lambda_r)} + \frac{[A]_r^*}{(p - \lambda_r^*)} \right) \tag{1.29}$$

Therefore the *residues* $[A]_r$, $[A]_r^*$ that can be written as:

$$[A]_r = ([H(p)](p - \lambda_r))|_{p=\lambda_r} \tag{1.30}$$

In the case of a MDOF system, it is important to introduce the concept of mode shape vectors ψ_r. These vectors represent the eigenvectors associated with the previously determined eigenvalues (as shown in Equation 1.27) and contain the modal displacement, which is expressed as a complex value.
After performing some calculations, it is possible to derive a relationship between the mode shape vectors ψ_r and the residues $[A]_r$, $[A]_r^*$. As a result, the transfer function can be expressed as:

$$[H(p)] = \sum_{r=1}^{N} \left(\frac{Q_r\{\psi\}_r\{\psi\}_r^T}{(p - \lambda_r)} + \frac{Q_r^*\{\psi\}_r^*\{\psi\}_r^{*T}}{(p - \lambda_r^*)} \right) \tag{1.31}$$

1.2.2 Frequency response function (FRF), Impulse response function (IRF)

Similar to the single degree of freedom case, the transfer function for the MDOF system can also be evaluated in both the frequency and time domains.
The *frequency response function* can be expressed as:

$$[H(j\omega)] = \sum_{r=1}^{N} \left(\frac{Q_r\{\psi\}_r\{\psi\}_r^T}{(j\omega - \lambda_r)} + \frac{Q_r^*\{\psi\}_r^*\{\psi\}_r^{*T}}{(j\omega - \lambda_r^*)} \right) \tag{1.32}$$

and the response is equal to:

$$\{X(j\omega)\} = [H(j\omega)]\{F(j\omega)\} \tag{1.33}$$

The *impulse response function* can be expressed as:

$$[h(t_s)] = \sum_{r=1}^{N} \left(Q_r\{\psi\}_r\{\psi\}_r^T e^{\lambda_r t_s} + Q_r^*\{\psi\}_r^*\{\psi\}_r^{*T} e^{\lambda_r^* t_s} \right) \tag{1.34}$$

and the response is equal to the convolution between the impulse response function and the forcing function:

$$\{x(t_s)\} = [h(t_s)] * \{f(t_s)\} \tag{1.35}$$

Chapter 2

Experimental Modal Analysis (EMA)

As previously stated, EMA is a modal analysis methodology that is based on measurements of dynamic input forces and output responses on the structure [14]. The modal parameter estimation and testing method used in this thesis study are introduced in this chapter.

2.1 Modal parameter estimation

Modal parameter estimation is a crucial step in the EMA process, over the past few years several methodologies have been developed and implemented. They have progressed from SDOF techniques to more complex MDOF approaches that analyze data from multiple input excitations and multiple output responses simultaneously. There are basically two categories of MDOF methods: one is based on the time domain, and the other is based on the frequency domain. Only the methodology employed in this work analysis is presented in the following.

The used methodology is a novel non-iterative frequency-domain parameter estimation technique, which utilizes a (weighted) least-squares approach and MIMO frequency response functions as primary data [16]. This approach, known as "PolyMAX" or polyreference least-squares complex frequency-domain method, can be executed similarly to the industry standard polyreference (time-domain) least-squares complex exponential method. Initially, a stabilisation diagram is created that includes frequency, damping, and participation information. A stabilisation chart is a tool that is frequently employed to distinguish between mathematical and physical poles. To generate a stabilisation chart, the analysis is repeated for ascending model order N, and the poles are computed from the estimated denominator coefficients for each model order. In the example (Figure 2.1) the stable poles can be seen graphically in ascending model order with the letter 's'; these poles correspond to the physically relevant modes, whereas the other poles are not constant and result from mathematical solutions without a physical interpretation, and are primarily caused by noise [17].

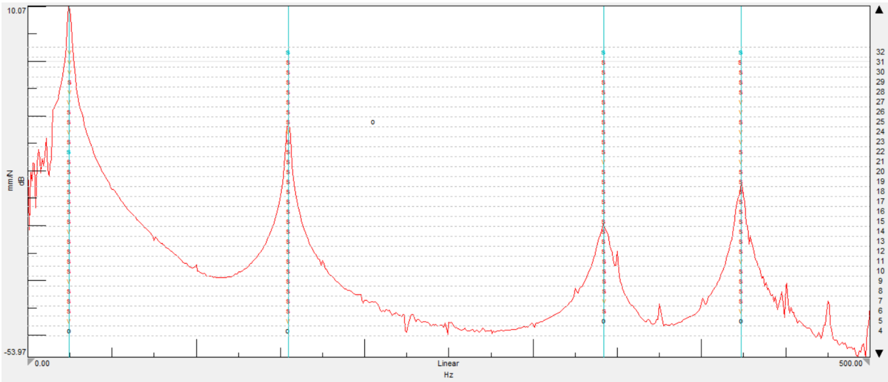

Figure 2.1: Stabilization diagram evaluated through PolyMAX

The mode shapes are subsequently determined in a second least-squares step, based on the user's selection of stable poles. The method's specific advantage is its stable identification of the system poles and participation factors as a function of the specified system order, resulting in easily understandable stabilisation diagrams. This feature offers the potential for automating the method and utilizing it for challenging estimation cases, such as high-order and/or highly damped systems with substantial modal overlap.

2.2 Testing techniques

The testing phase of EMA involves exciting the structure in order to measure the response and evaluate the FRFs, which allow the characterization of the dynamic behaviour of the analyzed structure. The purpose of exciting the structure is to generate a specific force level that excites the frequency range of interest. There are various methods of exciting the structure, including impact testing and shaker testing, both of which are briefly introduced in this section and were also used in the tests performed for the purpose of this thesis.

2.2.1 Impact testing

In impact testing, a hammer is used to strike the structure, generating an impact input that produces a relatively smoothly evolving force level up to a specific frequency. The energy level and the frequency span depends on the force of the user, the weight of the hammer, the hardness of the hammer tip and the compliance of the impact point on the structure. The closer the input force approximates a Dirac impulse (i.e., a signal with zero duration and infinite amplitude), the wider the frequency base band will be. The use of a hard-tip hammer, low hammer weight, low force, and a hard test object surface results in a short contact time and a signal that is close to a Dirac impulse, thereby exciting a higher frequency base band. Conversely, the use of a soft hammer tip and heavy hammer results in a longer contact time and lower frequency excitation. Therefore, this type of excitation is mainly employed for lightweight structures.

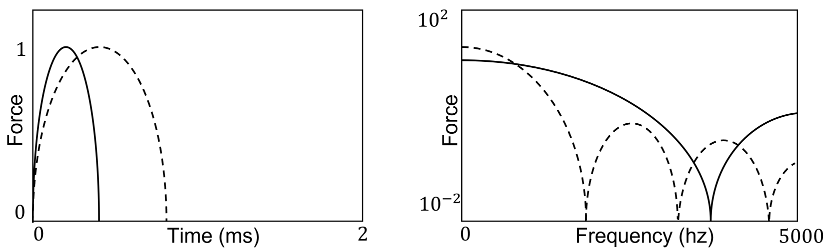

Figure 2.2: Hammer signals and their frequency content

Figure 2.3 depicts a typical excitation hammer, which consists of four main parts: the tip (1), which can be changed to excite a different frequency range; the force transducers (2), which enable the registration of the generated force signal; the balancing mass (3); and the handle (4). As this excitation system is not fixed, it has the advantage that it does not affect the dynamics of the object. However, on the other hand, the repeatability of the tests is more complex and may eventually require an "automatic" hammer.

Figure 2.3: Excitation hammer

2.2.2 Shaker testing

Another type of excitation method is provided by a shaker, which can be either fixed-fixed exciters when placed on the ground (or some frame) and attached to the test structure, or fixed exciters when attached only to the structure.The most commonly used fixed-fixed exciters are hydraulically and electrodynamically driven, with only the latter type being used in this work. The former type is typically used for higher displacement and lower frequency applications but is not very mobile due to its power supply requirements. The second type only requires an electricity supply, is more mobile and easier to use, and is able to reach higher frequencies and lower displacements. Figure 2.4 illustrates the scheme of an electrodynamic shaker, which consists of a moving coil assembly placed within a magnetic field and connected to a moving table that is then attached to the test object. An electronic control system provides the excitation signal, which is amplified and fed to the moving coil, thereby moving the test object.

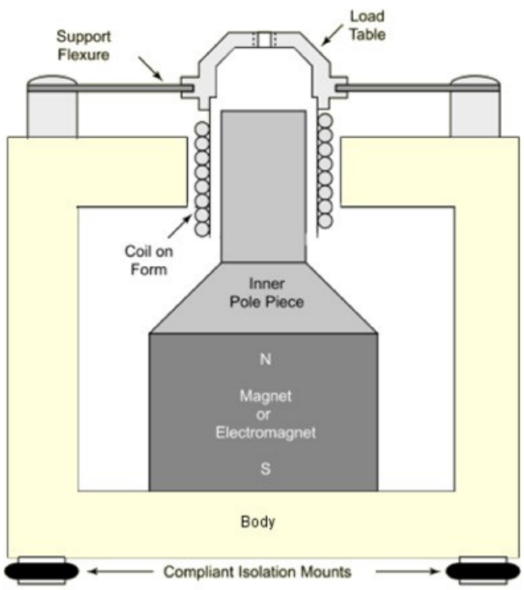

Figure 2.4: Scheme of an electrodynamic shaker

While using this kind of exciter, it's important to be mindful of the device's capacity because it's not always possible to replicate the input current or voltage's precise properties. This is because the input/output characteristics of the shaker are not uniform across the whole frequency range and because the mechanical impedance mismatch between the shaker and the test object causes the force to decrease during resonances.

Chapter 3

Signal Processing

Signal processing plays a critical role in the framework of Experimental Modal Analysis (EMA), as it is essential to measure both input and output data during the experimental procedure of a system subjected to external excitation, using appropriate transducers directly mounted on the structure. Commonly used sensors for structural testing include strain gauges, accelerometers, and load cells, which are capable of respectively converting displacements, accelerations, or forces into electrical signals. To enable the processing and analysis of these signals, it is necessary to convert them into digital signals, making digital signal processing a crucial tool for system analysis [14, 15]. Since this work deals with signal processing and related phenomena, in this chapter, after a brief signal classification, the main signal processing errors and the procedure to avoid and minimize them are described.

3.1 Signal classification

The classification of signals that may be utilised for signal identification is illustrated in Table 3.1. Signals that are stationary can either be deterministic or random and have average qualities that do not change over time. The most important group of deterministic stationary signals is the group of periodic signals. A pseudo-random signal consists of a random signal that is periodically repeated. Non-stationary can be separated into continuous and transient. Transient signals are those that begin and stop at zero during the observation time frame.

<table>
<tr><th colspan="4">signals</th></tr>
<tr><td colspan="2">stationary</td><td colspan="2">non-stationary</td></tr>
<tr><td>deterministic</td><td>random</td><td>continuous</td><td>transient</td></tr>
<tr><td>periodic
quasi-periodic</td><td></td><td rowspan="2"></td><td rowspan="2"></td></tr>
<tr><td colspan="2">psuedo-random</td></tr>
</table>

Table 3.1: Signal types

3.2 Errors and Windows

3.2.1 Aliasing

Aliasing is a phenomenon that originates from the fact that signals have to be sampled. It occurs when two continuous signals produce the same sequence of sample values when sampling at a certain frequency f_s. The Nyquist-Shannon theorem states that to completely resolve all the frequency content of a signal, it must be sampled at a rate that is twice the highest frequency present in that signal:

$$f_{max} < f_s/2 \tag{3.1}$$

where f_{max} is the highest frequency that characterizes the signal to be sampled and f_s is the sampling frequency. If this condition is not met, sampling a signal will lead to a degradation of the information that defines it. As an illustration, Figure 3.1 can be examined, which depicts a sine wave at a frequency of 6 Hz that represents the original signal to be sampled. When this signal is sampled at a rate of 5 Hz, the resulting signal will exhibit aliasing with a frequency of 1 Hz.

The aforementioned principle can be expressed more generally through the following equation:

$$f_a = nf_s \pm f_o \tag{3.2}$$

where f_a denotes the frequency of the resulting aliased signal obtained through sampling at a frequency of f_s, f_o refers to the frequency of the original signal and n represents an integer. Figure 3.2 visually demonstrates, as an example, how the aliased frequencies appear when the signal is sampled at a frequency of 5 Hz.

It is evident that the aliased frequency is equivalent to the original frequency only when $f_o < f_s/2$. To prevent aliasing, an anti-aliasing filter can be used. This filter processes the original time signal using a low-pass filter that eliminates frequencies above the Nyquist frequency, which is equal to half of the sampling frequency ($f_s/2$).

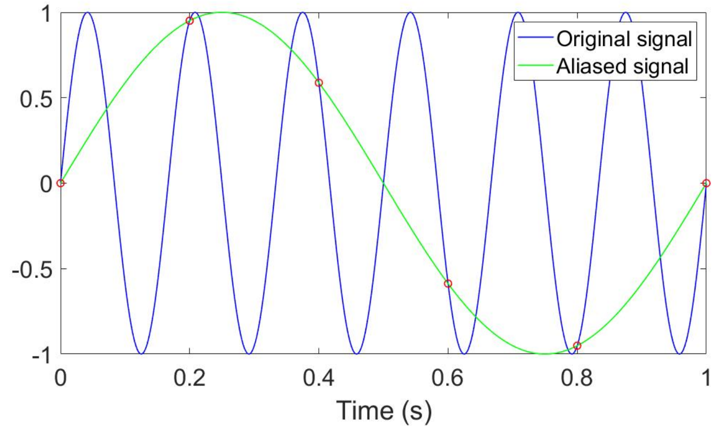

Figure 3.1: Aliasing example

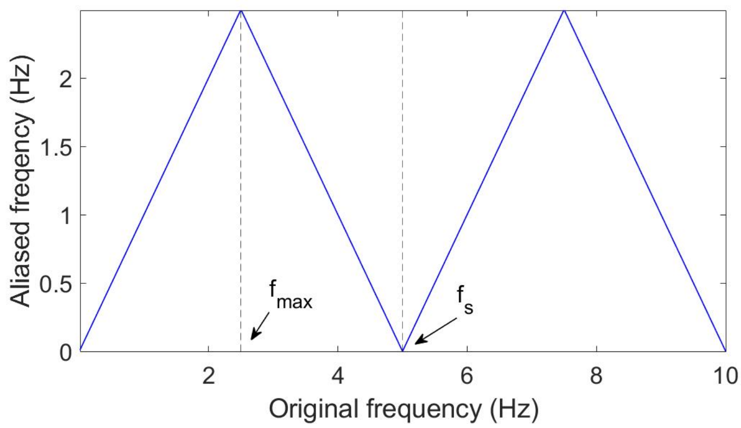

Figure 3.2: Aliased frequencies example for $f_s = 5Hz$

3.2.2 Leakage

Leakage errors arise due to the finite time interval T during which the measured signal is sampled. When a signal is sampled, the continuous-time signal is transformed into a continuous function of discrete variables. Since many algorithms for modal parameter analysis operates in the frequency domain, the Discrete Fourier Transform (DFT) is employed to obtain the spectrum of the measured signal. However, applying the DFT signals are assumed to be periodic, if this condition is not met, a leakage error occurs.

Figure 3.3 depicts an example of leakage comparing two distinct scenarios in which a signal is evaluated within a specified time window T. In the first case, a sine wave with a frequency of 2 Hz is evaluated within a time window of 2 seconds,

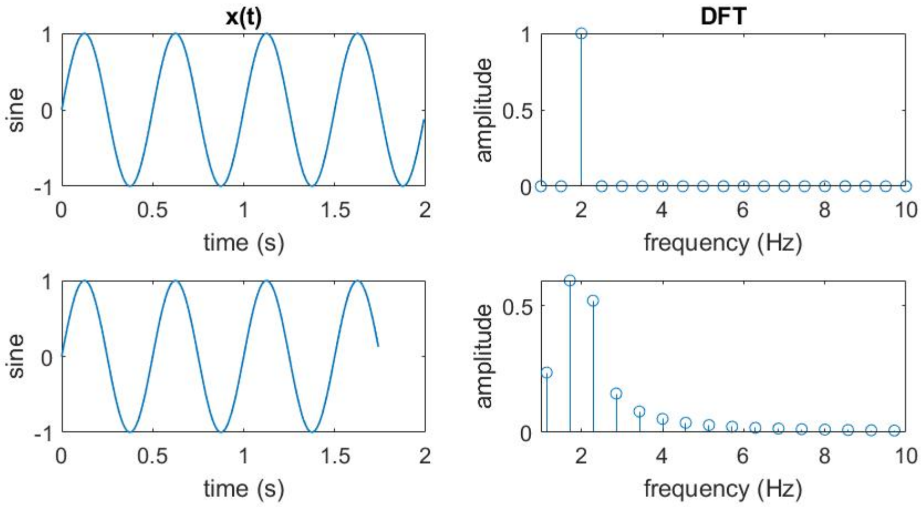

Figure 3.3: Leakage example

resulting in a periodic signal within that window. The corresponding discrete Fourier spectra, which assumes the periodicity of the signal within that window, produces a single line at the frequency of the cosine wave. In the second case, the same sine wave is evaluated within a time window of 1.75 seconds, hence the periodicity is not strictly valid since there is a discontinuity at the end of the time window. Upon analyzing the spectrum in this scenario, it is apparent how it is not the exact one, the energy of the signal is leaked to nearby frequencies, causing amplitude errors. Since any signal can be expressed as a linear combination of sine and cosine, the phenomenon observed in this example can be generalized for all signals. An appropriate solution to this problem is the utilization of suitable time windows.

3.2.3 Windows

In digital signal processing, it is not feasible to avoid the use of a time window, since when a signal is measured for a limited duration, it implies that a rectangular time window is applied to the signal. Nonetheless, choosing a more appropriate time window can significantly reduce the leakage error by imposing periodicity on the signal. Various types of windows are available that can be applied to the analyzed signal for different types of problems. The choice of the window is typically a trade-off between obtaining a good estimation of amplitude values and a high spectral resolution.

Figure 3.4 illustrates three different types of windows as examples. The first column displays the original signal, the second column shows the window function, and the third column shows the "windowed" signal obtained by applying the window to the original signal.The windowing process involves multiplying the signal by the window function element-wise. The mathematical expression for obtaining the "windowed" signal can be given as:

$$x_w(t) = x(t) \cdot w(t) \tag{3.3}$$

The three windows displayed in Figure 3.4 are: (1) Rectangular, (2) Hanning, and (3) Exponential. The rectangular window is the simplest type of window function, which can results in spectral leakage, particularly if the signal is not periodic within the time window. The Hanning window is a weighted function that gradually tapers the signal towards zero at the edges, and, like others non-rectangular windows, is used for continuous signals obtained through steady periodic or random excitation signals. The exponential window is suitable for transient vibration signals that are obtained, for example, through impact testing.

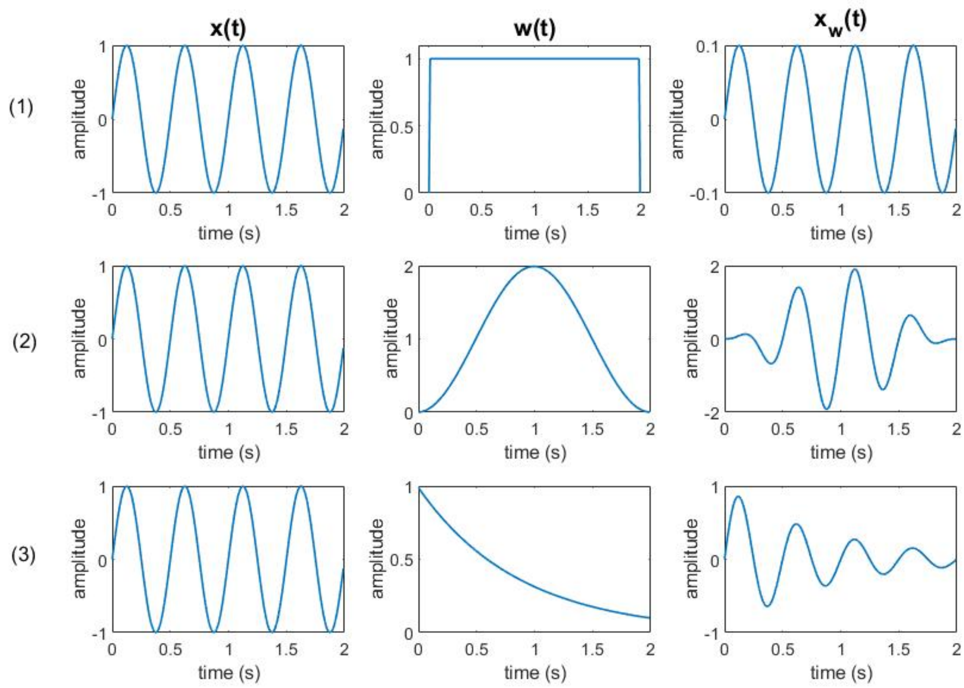

Figure 3.4: Windows examples

Chapter 4

Digital Imagine Correlation (DIC)

Digital Image Correlation (DIC) is an optical-numerical measuring technique which offers the possibility of determining complex shape, displacement and deformation fields at the surface of objects under any kind of loading. This system only requires one or more cameras and a speckled specimen, making it advantageous as it does not require wiring. Additionally, compared to other measuring techniques, it has the potential to provide spatially dense information [18].

DIC is a pattern tracking method that utilizes a random pattern, such as a drawn or applied speckle or natural texture, on the surface of the object being analyzed. The algorithm tracks the pixels by comparing a reference image with the deformed ones based on the pattern. Due to the limited information provided by individual pixels (n. of grey level), the algorithm uses subsets of pixels to track movement. The choice of pattern is dependent on various factors, including the camera lens used, the distance between the object and camera, and the object's dimensions. Prior to the correlation process, a Region Of Interest (ROI) is selected in the reference image, which is then divided into subsets. The size of the subset and the distance between each subset, known as the step size, are chosen as a trade-off to obtain sufficient points for spatially dense information while minimizing computation time. To obtain clear and accurate images of the structure and speckle, it is essential to ensure that the specimen is well illuminated and in focus, and that the contrast of the images is optimized.

4.1 Correlation process

The algorithm used to obtain displacement or deformation maps from DIC images involves a correlation process that tracks specific points between images to evaluate

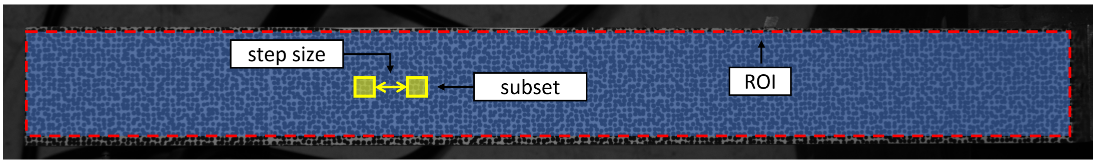

Figure 4.1: DIC reference image example

the displacement of each point over time. This correlation process consists of three main components: the matching criterion, interpolation, and shape function.

The *matching criterion* is the criteria used to correlate a subset in the reference image with the corresponding subset in the deformed image. This operation involves comparing the pixels that characterize each subset to find a match. There are various matching criteria that can be used, with two commonly used approaches being the *Sum Squared Difference (SSD)* and the *Zero Normalized Sum Square Difference (ZNSSD)*.
The SSD is the simplest one, it calculates the sum of squared differences between the corresponding pixel values in the reference and deformed subsets:

$$\chi^2 = \sum_i (G_i - F_i)^2 \tag{4.1}$$

The ZNSSD, on the other hand, normalizes the SSD by the mean and variance of the pixel values in the deformed subset:

$$\chi^2 = \sum_i \left(\left(\frac{\sum \bar{F}_i \bar{G}_i}{\sum \bar{G}_i^2} G_i - \bar{G} \frac{\sum \bar{F}_i \bar{G}_i}{\sum \bar{G}_i^2}\right) - (F_i - \bar{F}) \right)^2 \tag{4.2}$$

where χ is the function to be minimized, F the reference image subset, G the deformed image subset and i the i-th pixel in the subset. The mean value is indicated by a bar above the letters:

$$\bar{F} = \frac{\sum_i^n F_i}{n} \quad \bar{G} = \frac{\sum_i^n G_i}{n}$$

The choice between the two criteria depends on the quality of the lighting and the computational time available. The SSD can be more accurate but may be affected by reduced or shifted contrast, while the ZNSSD is more robust to such changes. However, the ZNSSD criterion takes more time. In the analysis that follows, we will use the ZNSSD criterion since it is more reliable.

The *interpolation* is a technique used to convert a discrete signal into a continuous signal, and in the correlation process, it allows for the estimation of information between pixels. Various kinds of interpolators are available, including linear, cubic polynomial, cubic spline, and optimized filter. Increasing the order of interpolation may lead to improved results, but it can also result in longer computational times. The selection of the appropriate interpolator depends on the specific situation. In any case, a good interpolator should match the values at the pixel locations, minimize amplitude and phase errors, and provide filtering.

The *subset shape function* is a function that is defined based on the behaviour of the structure. The selection of the shape function in the matching process determines how the subset can deform. For instance, an affine subset describes a linearly varying displacement field, while higher-order shape functions can describe more complex deformation fields. Figure 4.2 provides a mathematical description, illustrating how, in 2D, considering different terms leads to more complex shapes with high-order shape functions. However, utilizing more complex shape functions can result in more accurate solutions at the expense of longer computational time.

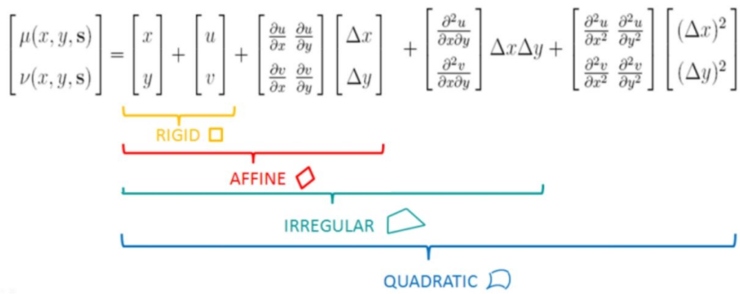

Figure 4.2: Mathematical description of the subset shape function

All of these components collectively characterize the correlation process that is used to obtain the displacement field from captured images [19].

4.2 Stereo DIC

DIC analysis can be performed with one or more cameras. With one camera, 2D analysis is conducted by correlating a set of images captured by the same camera, resulting in a 2D displacement field. However, this approach has restrictions: the specimen must remain flat, the camera must be perpendicular, and there should be no out-of-plane motion, which can be misinterpreted as in-plane motion.

Alternatively, 3D analysis can be performed using two cameras. In this case, the correlation process involves not only comparing the reference and deformed images from the same camera but also from two different cameras taken simultaneously. Figure 4.3 illustrates the multiple correlation processes involved. First, the horizontal correlation produces a pair of values (q and r), which do not correspond to physical displacements but instead are used to triangulate the position of the cameras in a suitable reference frame. Then, by adding the vertical correlation, the actual displacement can be evaluated, leading to a 3D displacement field.

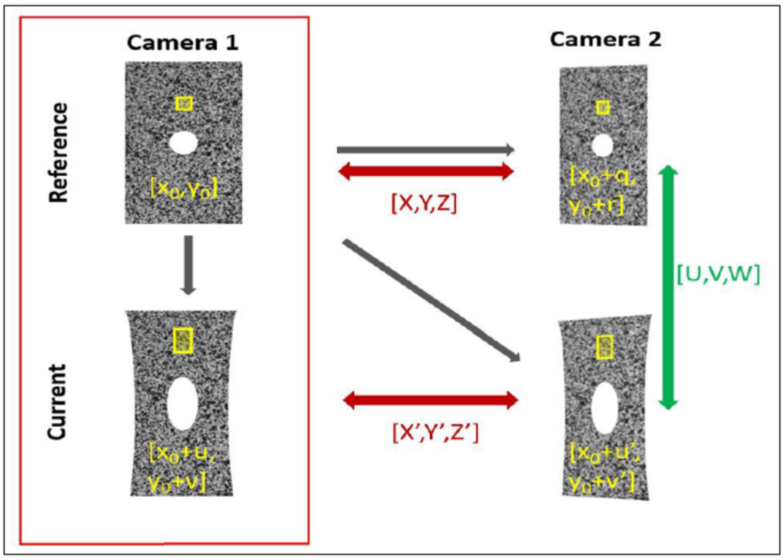

Figure 4.3: Stereo DIC multiple correlation process

Before conducting tests, calibration is necessary to determine the 3 translation and 3 rotation coordinates needed to transform from one camera frame to the other, as well as other parameters specific to each camera, such as focal length. A well-executed calibration process is essential for obtaining accurate results. During the testing phase, it is important to ensure that the cameras are at the same distance from the object, and the object is preferably positioned at the center of the two cameras. The choice of parameters such as stereo angle and focal length should strike a balance between accuracy of out-of-plane motion and matching errors.

Whether to use 2D or 3D DIC depends on the specific analysis needs. While stereo DIC can provide an additional dimension of information, the multiple correlation processes can also introduce more errors [19].

Part II

Random Sampling method

Chapter 5

Methodology Overview

This chapter provides an overview of the fundamental principles of the Random Sampling methodology. Section 5.1 describes the adopted sampling strategy, while Section 5.2 outlines the mathematical concepts of the optimization method. Finally, in Section 5.3, the feasibility of the optimization algorithm is demonstrated through a stability analysis.

5.1 Sampling strategy

In typical data acquisition, time data signals are collected at a fixed frame rate. However, in this case a random sampling scheme is adopted, meaning that each sample is taken at a random interval from the previous sample. To implement this approach, it is necessary to define a random sampling interval within which each sample can occur. The lower limit is set by the maximum camera frame rate Δt_{min}, while the upper limit is set to ensure sufficient samples for signal reconstruction and is defined as $2\Delta t_{min}$. Figure 5.1 illustrates how the acquisition method works, with the dashed lines representing regular sampling and the red lines indicating random sampling, which can occur in the acquisition interval between Δt_{min} and $2\Delta t_{min}$ from the previous sample. The acquisition scheme presented is used to randomly trigger the cameras.

The random sampling scheme eliminates the ambiguity of aliasing, as there is no direct relationship between the sampling frequency and the frequency of the original signal being sampled, as defined in Equation 3.2. However, since the sampling frequency is much lower than the frequency of the actual structural behaviour, an optimization method is required to reconstruct the complete behaviour from the sparse data points obtained through random sampling.

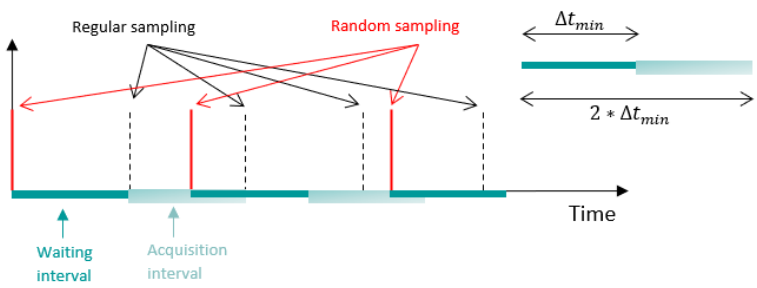

Figure 5.1: Random Sampling scheme

5.2 Optimization method

In Equation 1.34, the impulse response function (IRF) is defined for regular sampling. However, in the case of random sampling, it is necessary to define a new IRF in order to reconstruct the modal responses. By replacing the time variable t_s with the random sampling time t, the IRF for random sampling can be expressed as:

$$h(t) = \sum_{r=1}^{N} \Re(A_r e^{\lambda_r t}) \tag{5.1}$$

Here, A_r represents Q_r and ϕ_r, and can also be written as $A_r = \Re(A_r) + j\Im(A_r) = a_r e^{j\phi_r}$, where a_r is the amplitude and ϕ_r is the phase. The variable λ_r is given by $\lambda_r = 2\pi f_r j - \sigma_r$, where f_r is the natural frequency and σ_r is the damping factor.

The optimization algorithm aims to minimize the difference between the measured response and the theoretical response defined in Equation 1.35. To achieve this, the IRF defined in Equation 5.1 is substituted into Equation 1.35, and the squared residual between the measured response and the theoretical response is minimized in function of A_r and λ_r. This leads to the objective function:

$$\underset{A_r,\lambda_r}{\arg\min} = \sum_t \left[\sum_{r=1}^{N} \Re(A_r e^{\lambda_r t}) * f(t) - y(t) \right]^2 \tag{5.2}$$

where $y(t_r)$ is the measured response and $f(t)$ is the signal that defines the excitation force.

In the case of impact excitation, the objective function is simplified since the convolution between the IRF and the forcing function, which for an ideal excitation is a dirac function, is equal to the IRF. Resulting in the IRF being equal to the theoretical response, which, as the IRF suggests, can be decomposed into damped sine waves. By substituting A_r and λ_r, it is possible to define the objective function in terms of the four parameters $a_r, \phi_r, \sigma_r, f_r$:

$$\underset{a_r,\phi_r,\sigma_r,f_r}{\arg\min} = \sum_t \left[\sum_{r=1}^{N} a_r e^{-\sigma_r t} cos(2\pi f_r t + \phi_r) - y(t) \right]^2 \tag{5.3}$$

5.3 Stability Analysis

To assess the feasibility of this optimization, a stability analysis is performed to investigate the convexity of the objective function. For a simple case where the response is characterized by a single damped sine wave: $y(t) = \Re(e^{2\pi jt-t}) = e^{-t}cos(2\pi t)$, the objective function becomes:

$$g(a_r, \phi_r, \sigma_r, f_r) = \sum_t \left[\sum_{r=1}^{N} a_r e^{-\sigma_r t} cos(2\pi f_r t + \phi_r) - e^{-t} cos(2\pi t) \right]^2 \tag{5.4}$$

The solution of the minimization problem is:

$$N = 1 \quad a_1 = 1 \quad \phi_1 = 0 \quad \sigma_1 = 1 \quad f_1 = 1$$

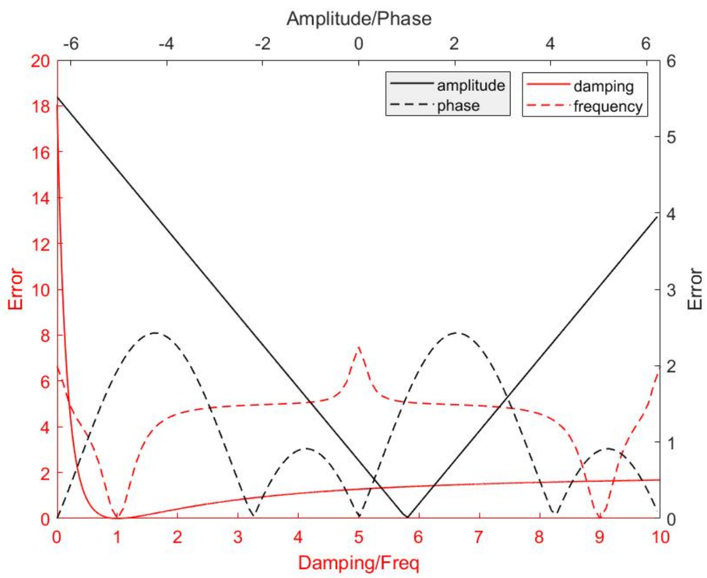

Figure 5.2: Objective function $g(a_r, \phi_r, \sigma_r, f_r)$ under perturbation

It is feasible to assess the convexity of the function with regard to these parameters by examining how perturbation in the four parameters impact the objective function g. Figure 5.2 demonstrates that the amplitude and the damping parameters are globally quasiconvex. Conversely, the phase and the natural frequency parameters do not exhibit a global minimum. Equation 5.3 represents a non-linear optimization problem that can be efficiently solved using a gradient-based algorithm with a warm start. An accelerometer can be employed to predict the natural frequencies and provide a preliminary estimate for f_r. While, it could be more difficult to provide a first estimate for the phase parameter. Therefore, an alternative approach to expressing the same objective function was explored.

By substituting a_r and ϕ_r, the objective function can be expressed as a function of $\Re(A_r)$, $\Im(A_r)$, σ_r and f_r, resulting in:

$$\underset{\Re(A_r),\Im(A_r),\sigma_r,f_r}{\arg\min} = \sum_t \left[\sum_{r=1}^{N} \Big[\Re(A_r)(e^{-\sigma_i t}cos(2\pi f_r t)\dots \right.$$
$$\left. -\Im(A_r)(e^{-\sigma_r t}sin(2\pi f_r t)\Big] - y(t)\right]^2 \quad (5.5)$$

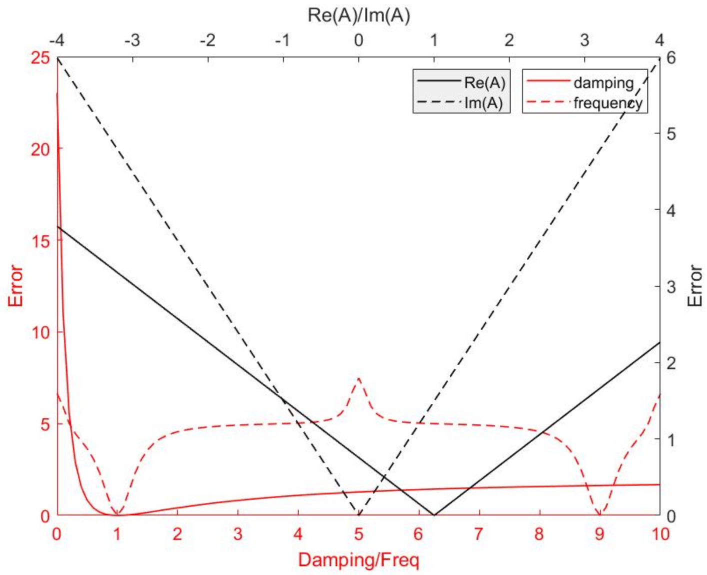

Figure 5.3: Objective function $g(\Re(A_r), \Im(A_r), \sigma_r, f_r)$ under perturbation

Performing the stability analysis for the same simple case described in Equation 5.4 using the objective function expressed in Equation 5.5 yields the result depicted in Figure 5.3. It can be observed that only the natural frequency parameter lacks a global minimum. Therefore, optimizing with respect to $\Re(A_r)$ and $\Im(A_r)$ instead of a_r and ϕ_r ensures quasiconvexity when an initial guess close to the global minimum for the natural frequency is provided. To solve the optimization problem, a trust-region-reflective algorithm is used, wherein the step size and search direction are determined based on the gradient of the objective function [20].

In the case of multiple damped sine waves, it cannot be ensured that quasiconvexity is preserved. In signal processing, this phenomenon is referred to as aliasing. The random sampling scheme proposed in this context can eliminate the ambiguity caused by aliasing, enabling the differentiation of the contribution of each damped sine wave.

Chapter 6

Numerical Validation

The first step to validate the random sampling methodology is done by performing a numerical simulation on multiple damped sine-waves. This chapter comprises an explanation of the validation algorithm in Section 6.1, followed by the presentation of the validation results in Section 6.2. In the final section, a slightly modified version of the algorithm is explained, and the corresponding results are displayed.

6.1 Algorithm

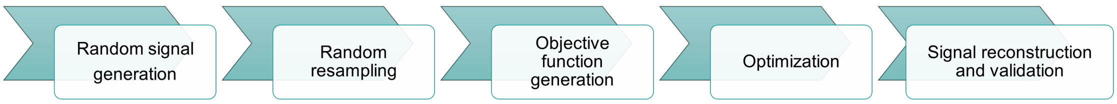

Figure 6.1: Numerical Validation Algorithm

The validation algorithm in Figure 6.1 has been implemented using MATLAB. Firstly, a signal representing the displacement of the structure is generated randomly. Assuming that the displacement can be decomposed into damped sine waves, as previously demonstrated, the signal is expressed as:

$$Y(t) = \sum_{r=1}^{N} \left[\Re(A_r)(e^{-\sigma_i t} cos(2\pi f_r t) - \Im(A_r)(e^{-\sigma_r t} sin(2\pi f_r t) \right]$$

Here, the values of $\Re(A_r)$, $\Im(A_r)$, σ_r, and f_r are randomly generated. Next, the signal is subjected to random sampling. This results in the extraction of $Y(t_{rand})$ from $Y(t)$, as depicted in the example in Figure 6.2. After that, the objective function 5.5 is generated, and a nonlinear problem is solved using a trust-region-reflective algorithm to obtain the optimized four parameters that allow evaluating the optimized displacement as a function of time. An initial guess for the natural frequency is provided, which is known from the randomly generated parameters. Then, a comparison is made between the original displacement generated in the first step and the optimized one, in both the time and frequency domains.

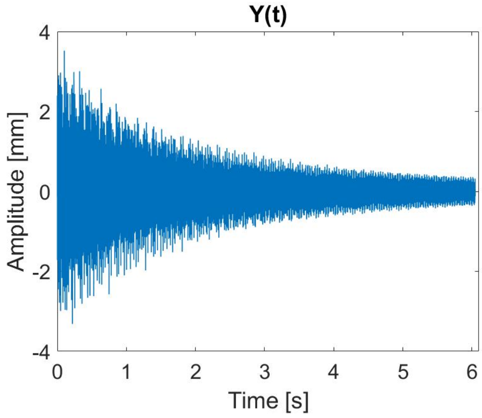

(a) Original

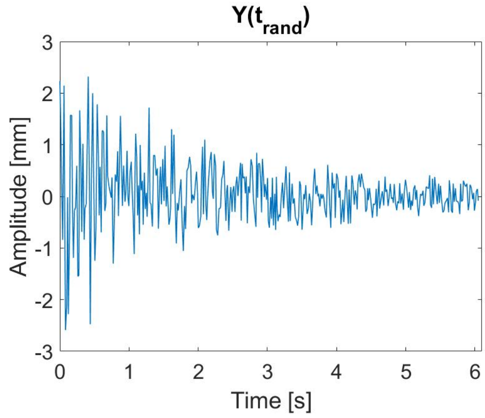

(b) Randomly sampled

Figure 6.2: Random signal generated

6.2 Results

This section presents the results of two validations. The first is conducted under ideal conditions, while the second is designed to simulate more realistic conditions by introducing noise and shifting the initial natural frequency guess provided to account for potential errors. The noise is added after computing the average signal-to-noise ratio (SNR) along the structure using data from prior experimental pre-tests, which is determined to be approximately 35 dB. Moreover, the shift of the natural frequency initial guess is set equal to half the frequency resolution. For both the validations, Table 6.1 presents the parameters necessary for generating and randomly sampling the signal.

To evaluate the accuracy of the optimization, a comparison between the optimized and original data is conducted using the following parameters:

- Mean Square Error (MSE) in the time domain
- Time Response Assurance Criterion (TRAC) in the time domain
- Frequency Response Assurance Criterion (FRAC) in the frequency domain

Random signal parameters	
N. modes	20
Natural frequencies	0 to 500 Hz
Damping factor σ_r	1e-4 to 1
Real part $\Re(A_r)$	-1 to 1
Imaginary part $\Im(A_r)$	-1 to 1
Frame rate	<100 Hz
Time interval	0.01 s to 0.02 s
Measured time	$\sim$ 6 s
N. samples	400

Table 6.1: Validation parameters

The MSE is calculated as follows:

$$MSE = \frac{1}{n}\sum_{i=1}^{n}(Y_i - \hat{Y}_i)^2 \tag{6.1}$$

where n represents the number of time points at which the signal is evaluated. The TRAC is given by:

$$TRAC = \frac{\left|Y \cdot \hat{Y}^T\right|^2}{|Y|^2 \cdot \left|\hat{Y}\right|^2} \tag{6.2}$$

while the FRAC is calculated as:

$$FRAC = \frac{\left|H \cdot \hat{H}^T\right|^2}{|H|^2 \cdot \left|\hat{H}\right|^2} \tag{6.3}$$

Here, Y refers to displacement, and H to the Fast Fourier Transform (FFT) of the displacement, and the symbol ˆ denotes the optimized data.
In addition, a percentage error is calculated for each parameter by comparing the original parameters used to generate the signal with the optimized ones:

$$error = \frac{|\langle\cdot\rangle_{ref} - \langle\cdot\rangle_{opt}|}{\langle\cdot\rangle_{ref}} \cdot 100 \tag{6.4}$$

Figures 6.3 and 6.4 present the graphical results obtained from comparing the original and optimized displacements, as well as the parameter errors as a function of the optimized modes. Table 6.2, on the other hand, displays the comparison results in terms of MSE, TRAC, and FRAC.

In the validation where ideal conditions are considered, it can be observed that by considering a response characterized by 20 modes in a frequency range of 0 to 500 Hz, the optimization process successfully recovers the original displacement in both the time and frequency domains. The TRAC and FRAC are both equal to one and the MSE is lower than the squared amplitude of all damped sine waves.

In the real condition validation, a lower MSE is observed, although it remained lower than the squared amplitude of all damped sine waves, and a high value of TRAC and FRAC is obtained. Despite a substantial increase in errors compared to ideal conditions, the errors are still reasonable. It was observed during other validations that the accuracy of the optimization process decreases as the damping factor of the modes characterizing the signal increases.

The results in both cases are considered acceptable since a sampling frequency of 100 Hz was used to reconstruct modes up to 500 Hz. It is worth noting that from the Nyquist-Shannon theorem to recostruct modes up to 500 Hz imposes a sampling frequency of 1000 Hz.

Ideal condition results	
MSE	5.53e-15
TRAC	1
FRAC	1

Real condition results	
MSE	2.58e-4
TRAC	0.99
FRAC	0.99

Table 6.2: Optimization comparison results

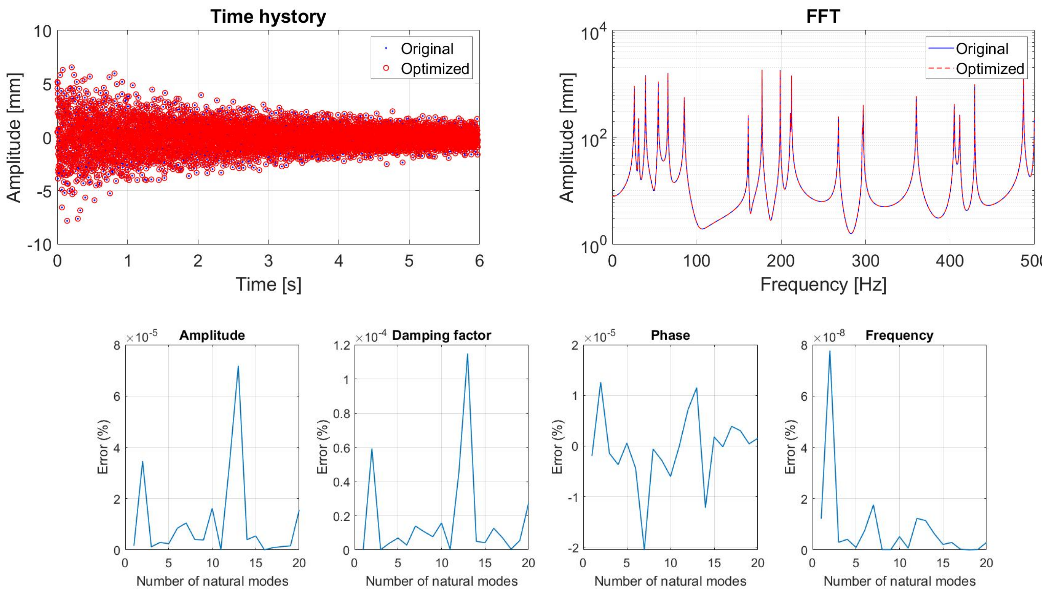

Figure 6.3: Ideal condition graphical results

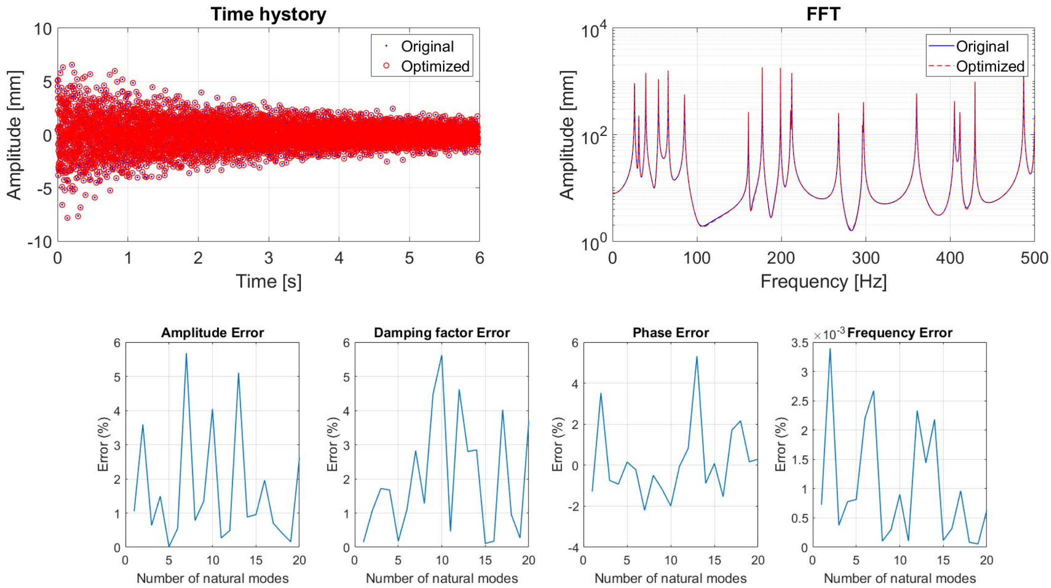

Figure 6.4: Real condition graphical results

6.3 Alternative algorithm

This section introduces a slightly different algorithm, which was proposed based on observations made during the experimental validation process.

During the optimization process, it is essential to fix boundaries of the optimization problem. For the natural frequency f_r, the boundaries are defined around the known initial guess. However, for $\Re(A_r)$, $\Im(A_r)$ and σ_r larger boundaries can be set. As demonstrated in Section 5.3 these parameters exhibit quasiconvexity. During the experimental validation, it was observed that while the aforementioned property holds for the parameters $\Re(A_r)$ and $\Im(A_r)$, it is more complex for the damping factor σ_r because the optimization for this parameter is less accurate.

As the boundaries set during the numerical phase are the same ones used to produce the signal, this does not present a substantial problem. However, during the experimental phase setting the boundaries can be challenging, given that the damping factor of the structure is not known beforehand. Also, as indicated in Equation 1.12, the damping factor and the natural frequency are related. This dependence exacerbates the problem further. Rewritten in terms of f_r, Equation 1.12 becomes:

$$\sigma_r = \zeta_r \Omega_{n,r} = \zeta_r f_r 2\pi \tag{6.5}$$

(It should be noted that in this form, the sign of the damping factor is missing, since damping is considered without sign).

To overcome this limitation, the optimization algorithm was modified, using the damping ratio ζ_r as the optimization parameter, since it is not dependent on the natural frequency, instead of σ_r. This makes it easier to set boundaries during the experimental phase. By substituting Equation 6.5 into Equation 5.5, it is possible to derive the following objective function:

$$\underset{\Re(A_r),\Im(A_r),\sigma_r,f_r}{\arg\min} = \sum_t \left[\sum_{r=1}^{N} \left[\Re(A_r)(e^{-\zeta_r f_r 2\pi t} cos(2\pi f_r t) \dots \right.\right.$$
$$\left.\left. - \Im(A_r)(e^{-\zeta_r f_r 2\pi t} sin(2\pi f_r t)\right] - y(t)\right]^2 \quad (6.6)$$

Several validation attempts were conducted to compare the optimization algorithms using σ_r and ζ_r. It was determined that the optimization process using σ_r is more reliable in terms of optimizing more modes and it requires less computational time. For up to 10 modes, the results in terms of MSE, FRAC, and TRAC are comparable between the two methods, but increasing the number of modes leads to a better optimization using σ_r. On the other hand, using ζ_r proves to be advantageous to set the boundaries, particularly when the damping range is larger. Therefore, the choice between the two optimization algorithms was made depending on the experimental conditions.

As an example, the results of two validations performed with the same parameters, as illustrated in Table 6.3, are shown in Table 6.4. The number of modes has been changed in comparison to the previous validations due to the limitations of the optimization process using ζ_r, as well as the maximum frame rate being set to 75 Hz in order to replicate the conditions of the experimental tests that will be shown in the following chapter.

Random signal parameters	
N. of modes	15
Natural frequencies	0 to 500 Hz
Damping factor σ_r	1e-4 to 1
Real part $\Re(A_r)$	-1 to 1
Imaginary part $\Im(A_r)$	-1 to 1
Frame rate	<75 Hz
Time interval	0.0133 s to 0.0267 s
Measured time	$\sim$ 8 s
N. samples	400

Table 6.3: Validation parameters

Optimization process with σ_r	
MSE	3.25e-05
TRAC	0.99
FRAC	0.99

Optimization process with ζ_r	
MSE	0.02
TRAC	0.97
FRAC	0.97

Table 6.4: Optimization comparison results

Chapter 7

Experimental Validation

This chapter covers the experimental tests performed to practically confirm the approach after numerically demonstrating its efficacy. Section 7.1 provides a brief explanation of the experimental procedure, while Section 7.2 introduces the setup used, along with all its devices. The results obtained from validating the methodology using high speed and low speed cameras are presented in Sections 7.3 and 7.4, respectively. Finally, Section 7.5 compares the optimization process used in this work with the one used by the KU Leuven research group in a similar study.

7.1 Algorithm

In the experimental phase, the algorithm used is the same as the one employed in the numerical phase, with the exception that the input signal is not numerically generated but experimentally acquired. The cameras are randomly triggered. The first guess on the natural frequencies is provided by using an additional accelerometer.

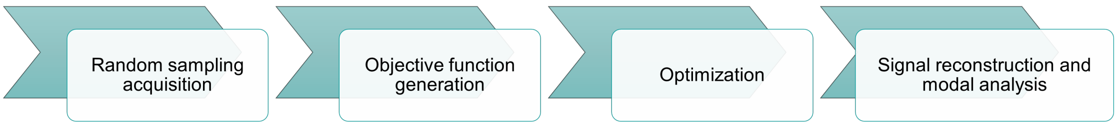

Figure 7.1: Experimental Validation Algorithm

7.2 Set-up

In Figure 7.2, a simple flowchart with the hardware used in the experimental measurement campaign is shown.

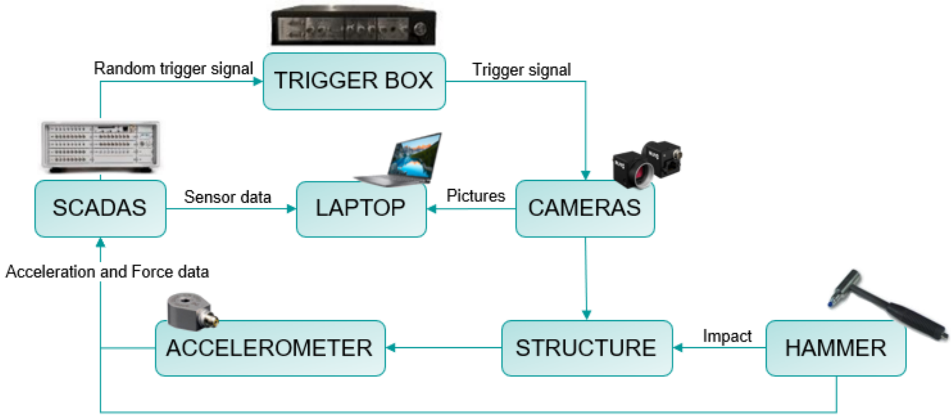

Figure 7.2: Set-up scheme for Random Sampling

The specimen analyzed in this study is an *aluminum beam* with dimensions of 400x40x4 mm. To simulate a cantilver beam, the structure was fixed on one side to an heavy mass and was let free on the other side. An appropriate speckle, as described in Chapter 4, has been glued on the surface. To obtain the natural frequency, an *uniaxial accelerometer* is used. The accelerometer was placed accordingly to avoid node lines for the first 4 modes. A *hammer* with a soft tip was used to excite up to 500 Hz. The *SCADAS* is used to acquire acceleration and force data from both the accelerometer and the load cell contained in the modal hammer. The SCADAS has also the function to send the trigger signal, which is a rectangular signal generated to have a random sampling scheme as described in Section 6. From the SCADAS the signal is sent to the *Triggerbox*, which then transmits it to the cameras. Two *stereo cameras*, whose specifications are listed in Table 7.1, capture images of the structure and transmit both the images and their timestamps to the laptop. In addition, the *laptop* also receives all the sensor data from the SCADAS. *Lights* are needed to properly illuminate the specimen.

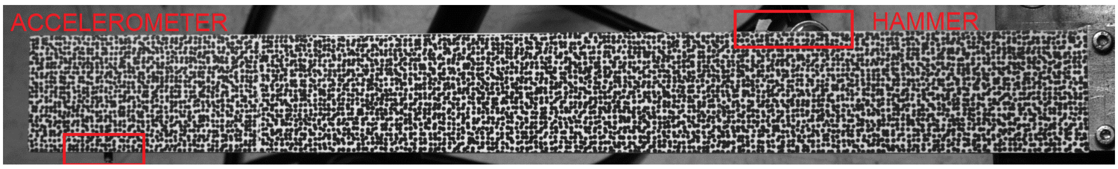

Figure 7.3: Test picture of the beam for low-speed camera validation

On the software side, the signals and images were acquired using the Siemens Simcenter Testlab acquisition software.

(a) Accelerometer (b) Modal hammer (c) SCADAS and Triggerbox

Figure 7.4: Used devices

Figure 7.5: Set-up complete for Random Sampling

Although the set-up described includes low-speed cameras, the initial experimental validation was conducted using high-speed cameras. This was done to more thoroughly validate the optimisation technique, using the original displacement captured with a sampling frequency above the Nyquist-Shannon limit as a comparison for the optimized displacement. However, the ultimate goal of the thesis is to use low-speed cameras for these analyses. Therefore, a second validation using low-speed cameras is performed.

Blackfly S BFS-U3-51S5M	
Resolution	2448 x 2048 pixels
Pixel size	3.45 μm x 3.45 μm
Maximum fps full resolution	75 fps
Bit depth	8 bit

Table 7.1: Low-speed camera specifications

Figure 7.6: Blackfly S BFS-U3-51S5M

i-Speed 5 Series 510	
Resolution	1920 x 1080 pixels
Pixel size	13.5 μm x 13.5 μm
Maximum fps full resolution	4980 fps
Bit depth	8 - 12 - 16 bit

Table 7.2: High-speed camera specifications

Figure 7.7: i-Speed 5 Series 510

7.3 High-speed camera validation

For the aforementioned reasons, the first step of the experimental procedure to evaluate the methodology consisted of performing a test with high-speed cameras to obtain reference results in terms of displacement, FRFs, and mode shapes. Then, the captured displacement from this test is randomly sampled to optimize it with the proposed method, and the results are compared.

In Table 7.3, the report for the high-speed camera test is shown, including all camera settings and correlation parameters used for post-processing (as explained in Chapter 4). The exposure time was set to provide sufficient brightness while being compatible with the required frame rate to capture the structural behaviour. The stereo angle was determined through several trials to find the optimal configuration. The length of the portion of the beam that the cameras are capturing is 358 mm, hence the resolution is 0.19 mm/pixel. It is worth noting that the speckle used for this validation is different from the one used in the low-speed camera validation, as different lenses were used. This difference can be seen by comparing Figure 7.3 with Figure 7.8.

Camera Settings	
Noise std	0.0056 mm
Focal length	50 mm
Object-camera distance	$\sim$ 1 m
N. of images	21800
Pixel to mm	0.19
ROI	1940x400 pixels
Frame rate	3200 Hz
Exposure time	30 μs
Stereo angle	22°

DIC Settings	
Subset size	29 pixels
Step size	17 pixel
Correlation	ZNSSD
Interpolation	Local bicubic spline
Shape function	Quadratic

Table 7.3: High-speed camera validation test report

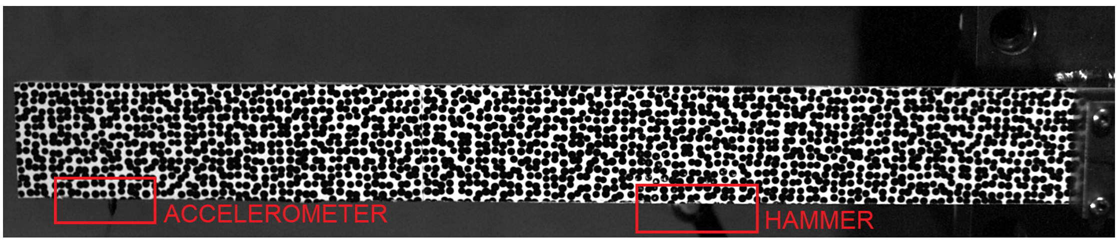

Figure 7.8: Test picture of the beam for high-speed camera validation

Processing the acquired images using Simcenter Testlab DIC Analysis made it possible to obtain the out-of-plane displacement for all the points that resulted from the subset and step size choice. By knowing the impact force, which is acquired

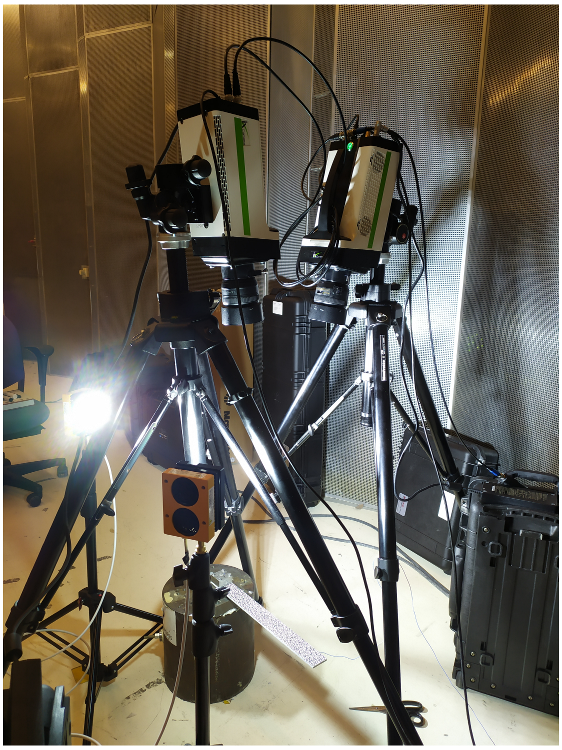

Figure 7.9: Set-up complete for Random Sampling with high-speed camera

during the test, it was possible to evaluate the FRF for each point and obtain the FRF sum. Consequently, Polymax is used to derive the mode shapes. The reference mode shapes that characterize the structure in the frequency range from 0 to 500 Hz are shown in Figure 7.10.

In order to validate the optimization method, the next step was to randomly sample the displacement obtained to get the reference results and optimize it using the algorithm described. Multiple optimization processes were carried out to better understand the limits of the method. Parameters such as the average random sampling frequency, the number of optimized modes, and the damping ratio boundaries were varied. In all of these optimization processes, the objective function optimized was the one shown in Equation 6.6, as optimizing ζ_r allowed for better boundary settings and resulted in improved results.

Figures 7.11 and 7.12 show the results of the first optimization process. In this case, only the first mode was accurately reconstructed, while the second mode had a shape closer to the correct one, but with a phase error at the edge. The third and fourth modes were completely inaccurate, as can be seen both from the mode shapes (Figure 7.11) and in the FFT comparison (Figure 7.12). The FFT is shown instead of the FRF because the optimization process assumed a unitary impact

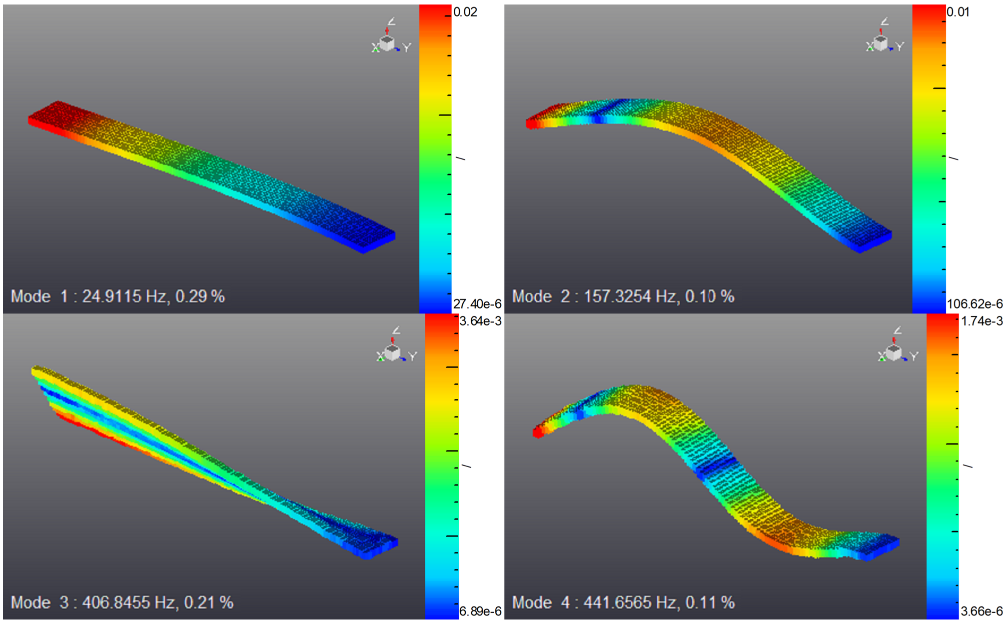

Figure 7.10: Reference mode shapes from high-speed camera test

force, so the FRF is equal to the FFT. As reported in Table 7.4, in this case, four modes are optimized and the random sampling is characterized by a maximum frequency of 75 Hz. The damping ratio boundaries were set based on the reference damping ratio, as it was observed that the optimization is highly sensitive to this parameter.

Optimization process parameters	
Damping ratio	1e-4 – 0.005 (max 0.5%)
Frame rate	< 75 Hz
Time interval	0.0133 s – 0.0267 s
Mearurament time	~5 s
N. of samples	250
N. of optimized modes	4

Table 7.4: Optimization parameters - 1st Optimization

To investigate the optimization results, the TRAC and the FRAC are evaluated for each point of the structure, comparing the reference data with the optimized one (see Figure 7.13). As expected, the optimization performs better farther from the clamp, where the structure is more steady and the behaviour is less like a sum of damped sine waves. However, in the main part of the structure, both the TRAC and the FRAC are about 0.8, illustrates well how only a portion of the

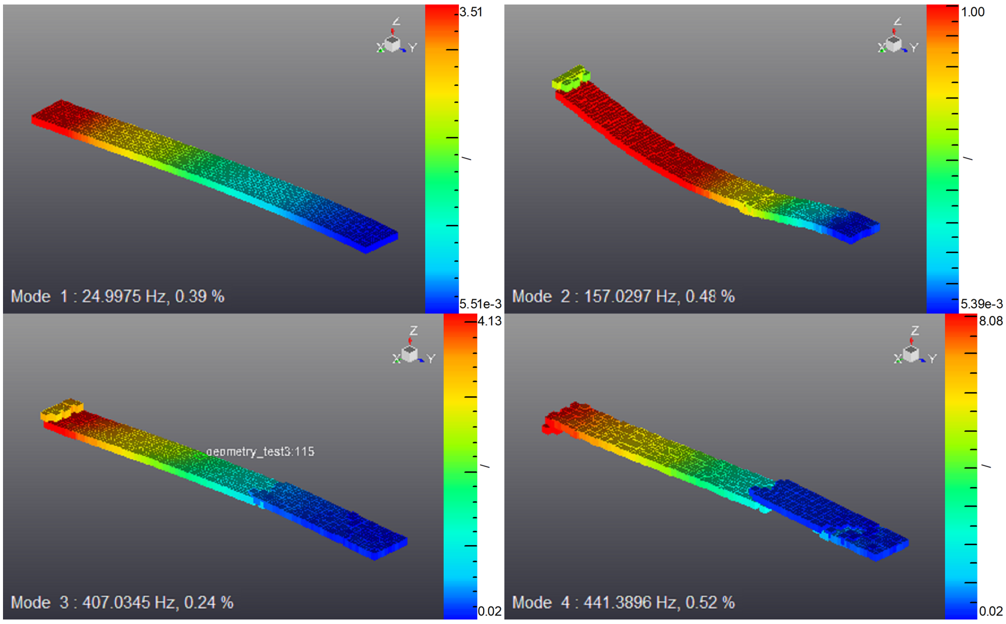

Figure 7.11: Optimized mode - 1st Optimization

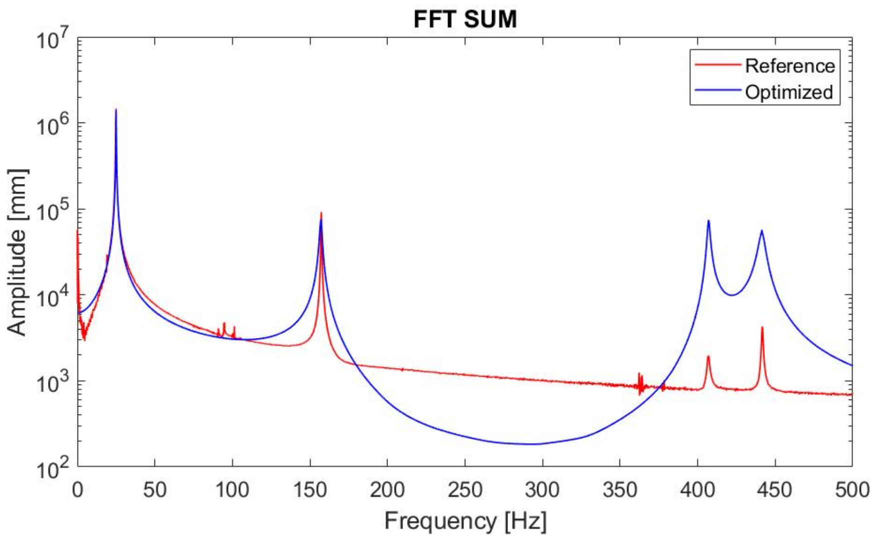

Figure 7.12: FFT comparison - 1st Optimization

behaviour is reconstructed. Additionally, Figure 7.14 shows a comparison between the reference data and the optimized results in terms of displacement and FFT for a single point at the edge of the structure (as shown in Figure 7.15). It can be seen that optimizing four modes, while the third and fourth modes are not well recognized, leads to the optimization converging on modes with high amplitude and high damping for the latter modes. This is why, in the first few instants of time history, the optimized displacement is far from the reference one.

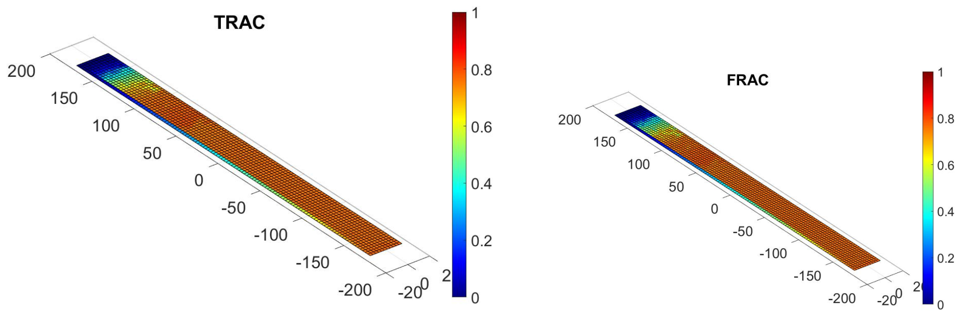

(a) TRAC (b) FRAC

Figure 7.13: TRAC and FRAC analysis for all the points

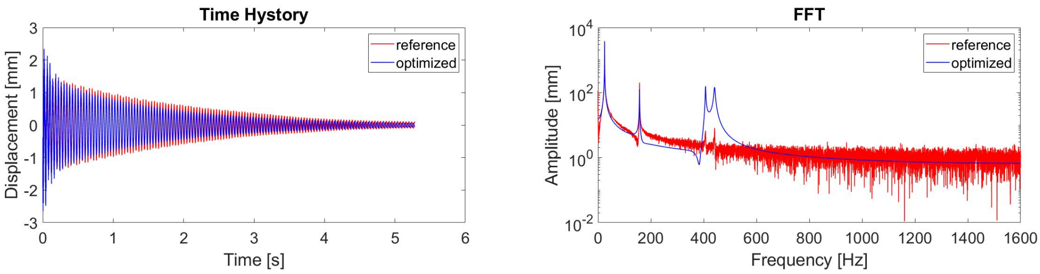

(a) Displacement (b) FFT

Figure 7.14: Example for a single point on the edge

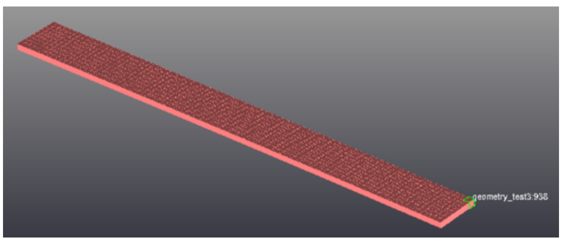

Figure 7.15: Structure scheme with the example point highlighted

Therefore, in the second and third optimization processes, only two modes were optimized in an attempt to better optimize the second mode. Figures 7.16 and 7.17 show the results of optimizing two modes with a maximum random sampling frequency of 75 Hz, while Figures 7.18 and 7.19 show the results of optimizing two modes with a maximum sampling frequency of 160 Hz. Optimizing fewer modes and increasing the frequencies led to better results, as can be seen from both the FFT comparison and the mode shapes.

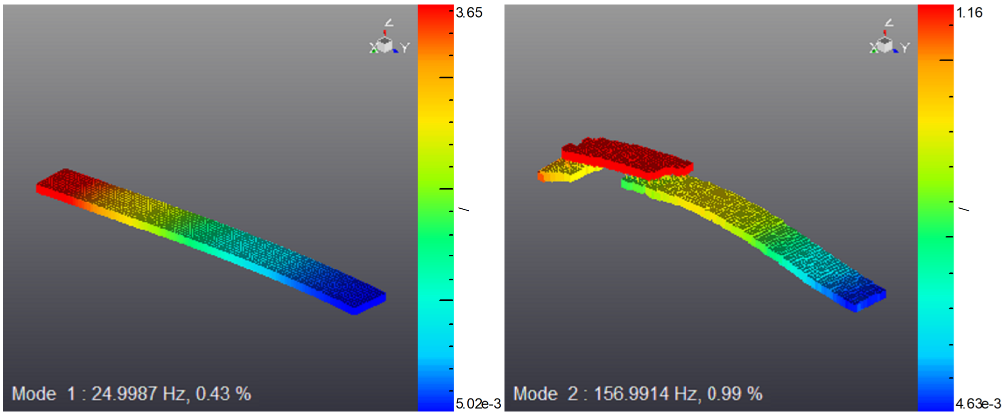

Figure 7.16: Optimized mode - 2nd Optimization

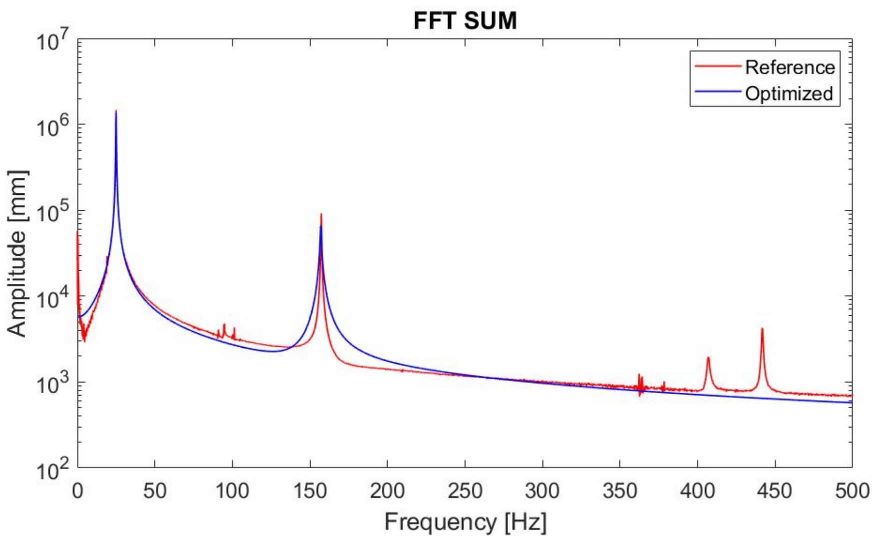

Figure 7.17: FFT comparison - 2nd Optimization

Optimization process parameters	
Damping ratio	1e-4 – 0.01 (max 1%)
Frame rate	< 75 Hz
Time interval	0.0133 s – 0.0267 s
Mearurament time	∼5 s
N. of samples	250
N. of optimized modes	2

Table 7.5: Optimization parameters - 2nd Optimization

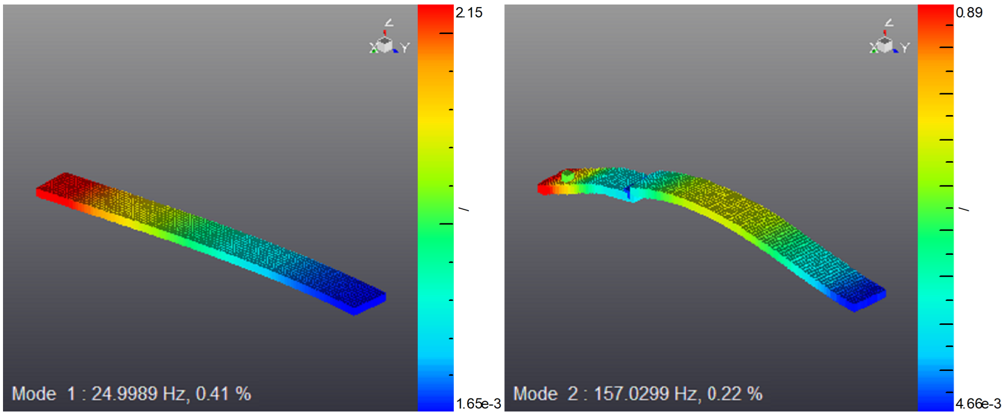

Figure 7.18: Optimized mode - 3rd Optimization

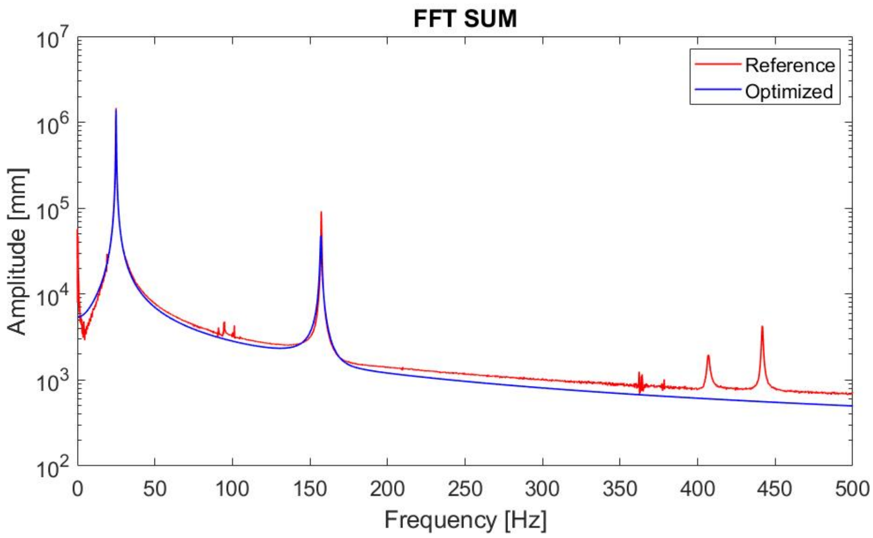

Figure 7.19: FFT comparison - 3rd Optimization

Optimization process parameters	
Damping ratio	1e-4 – 0.01 (max 1%)
Frame rate	< 160 Hz
Time interval	0.0063 s – 0.0126 s
Mearurament time	∼5 s
N. of samples	500
N. of optimized modes	2

Table 7.6: Optimization parameters - 3rd Optimization

7.4 Low-speed camera validation

The approach was also tested also low-speed cameras, mainly as they can give better resolution, despite the findings from the high-speed camera validation being not so precise in reconstructing the modes.

In this scenario, another test is performed. The camera is randomly triggered with a signal previously generated, with a maximum frame rate of 70 Hz, compatible with their capacity . The exposure time is increased to obtain more brightness in accordance with the frame rate, as dimmer lighting is used in this set-up. The other parameters are set as previously explained and listed in Table 7.7.

Camera Settings	
Noise std	0.0052 mm
Focal length	25 mm
Object-camera distance	∼ 1 m
N. of images	500
Pixel to mm	0.15
ROI	2416x376 pixels
Max. frame rate	70 Hz
Exposure time	600 μs
Stereo angle	18°

DIC Settings	
Subset size	23 pixels
Step size	15 pixel
Correlation	ZNSSD
Interpolation	Local bicubic spline
Shape function	Quadratic

Table 7.7: Low-speed camera validation test report

The acquired displacement is optimized after the processing of the randomly captured images. The optimized parameters are then used to derive a highly sampled optimized displacement, and the reconstructed modes are evaluated through Polymax. As a result of this procedure, there are no reference results of the same test available for comparison.

Only the results from one optimization process are presented for this test, as they were found to be relatively consistent with the validation from the high-speed camera. Table 7.8 displays the optimization parameters, while Figures 7.20 and

7.21 show the mode shapes and FFT results, respectively. In this case, even though four modes are considered, a better mode shape is obtained for the second mode, considering the lower average sampled frequency. This could be attributed to the slightly improved camera resolution. However, even using low-speed cameras, the ability of the optimization process to accurately reconstruct the modes is limited to a certain frequency range.

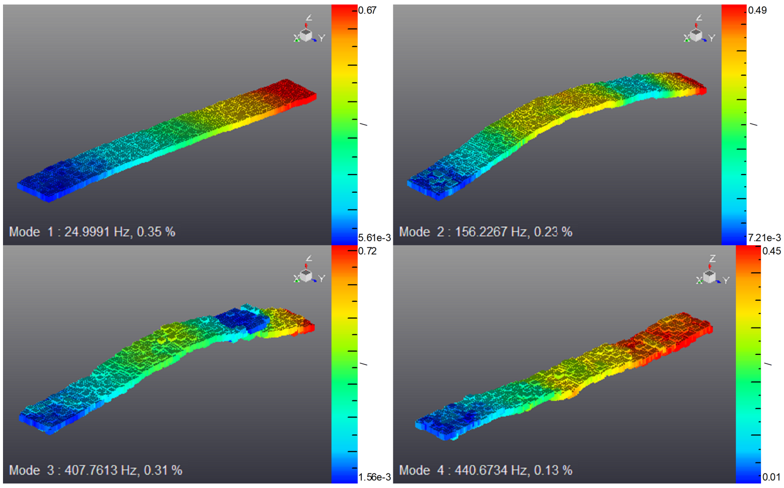

Figure 7.20: Optimized mode - Low-speed camera optimization

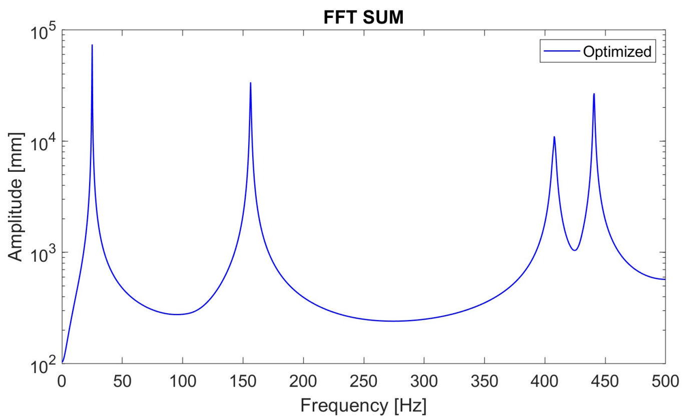

Figure 7.21: FFT - Low-speed camera optimization

Optimization process parameters	
Damping ratio	1e-4 – 0.01 (max 1%)
Frame rate	< 75 Hz
Time interval	0.0133 s – 0.0267 s
Mearurament time	∼5 s
N. of samples	250
N. of optimized modes	2

Table 7.8: Optimization parameters - Low-speed camera optimization

7.5 KU Leuven test comparison

In addition to the previous tests presented, in collaboration with the KU Leuven, the proposed methodology and algorithm are further validated through the application of the optimization process to a different test conducted by the research group at KUL.

While a detailed description of the experimental test can be found in [10], a brief summary is provided here for the purpose of comparison between the two experimental methods. The experimental test involved a beam fixed in a clamped-clamped configuration, as depicted in Figure 7.22. Only one camera was employed as a 2D analysis was performed to evaluate the in-plane displacement. To process the displacement data, the Lucas-Kanade optical flow method was used instead of DIC. Furthermore, to reduce noise, a median filter in space was applied to average the displacement data. The specifications of the camera used can be found in Table 7.9.

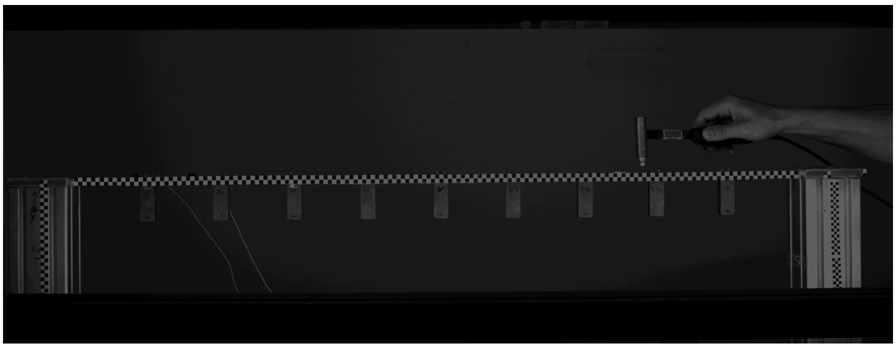

Figure 7.22: KUL test set-up

Similar to the previously described procedure, the processed and filtered displacement data obtained from randomly sampled images is optimized to evaluate the optimized parameters and obtain the optimized displacement data. The resulting

Ximea xiB-64 CB120RG-CM-X8G3	
Resolution	4096 × 3072 pixels
Pixel size	5.5 μm x 5.5 μm
Maximum fps full resolution	66 fps
Bit depth	12 bit

Table 7.9: KUL test camera specifications

mode shapes were then obtained through the use of Polymax.

In Table 7.10 are listed the optimization process parameters. It is to be noted that in this case was used the objective function 5.5 since the damping characteristics of the structure allowed to better optimize the displacement using σ_r instead of ζ_r.

Optimization process parameters	
Damping factor	1e-4 – 1
Frame rate	$<$ 50 Hz
Time interval	0.02 s – 0.04 s
Mearurament time	$\sim$5 s
N. of samples	169
N. of optimized modes	8

Table 7.10: Optimization parameters - KUL data optimization

Figures 7.23 and 7.24 provide a comparison between the optimized results obtained through this work and the results optimized by KUL in terms of FFT and mode shapes. Figure 7.24 displays the modes optimized by the KUL research group on the lef, and the modes optimized using the process described in this work on the right. It can be observed that the results obtained are similar in both cases. It is important to note that in this test, since the conditions were favorable, the first five modes were roughly reconstructed. However, the remaining three modes, which characterize the structure, were not shown as their mode shapes lacked physical meaning.

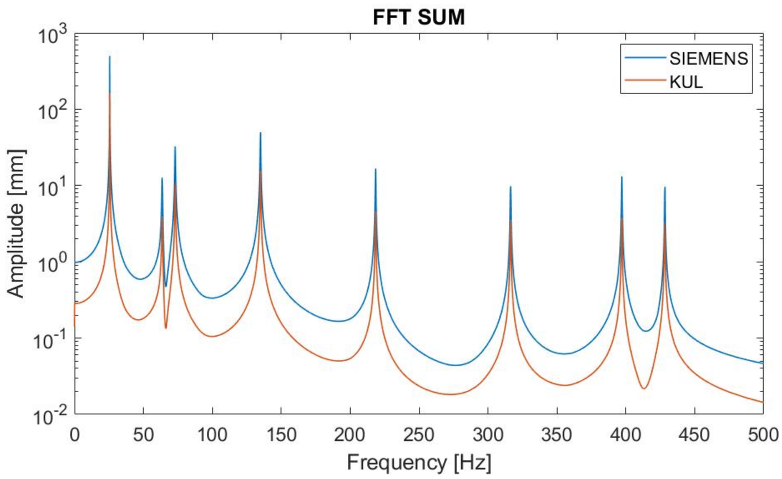

Figure 7.23: FFT comparison

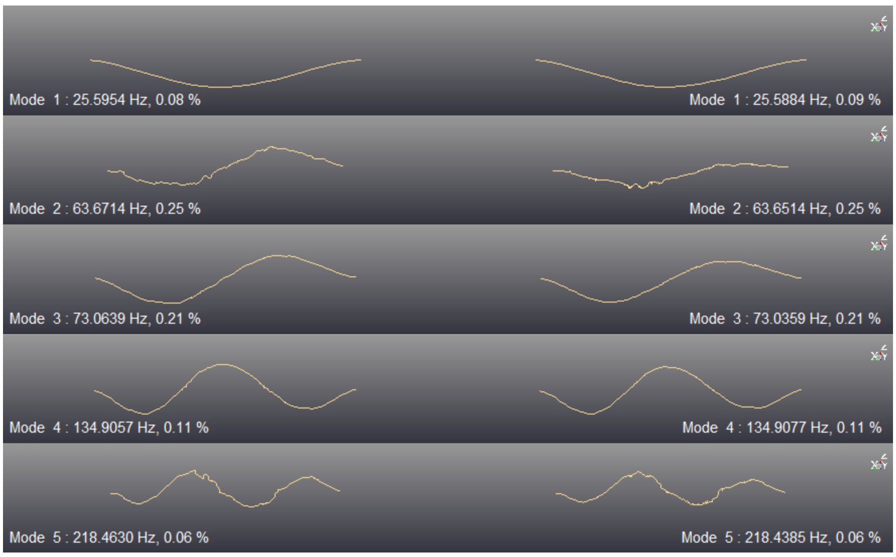

Figure 7.24: Mode shapes comparison

Part III

Smart Aliasing method

Chapter 8

Methodology overview

During shaker testing, the number of excitation cycles required can vary depending on the desired number of averages to be considered or the need to wait for the transient response to dissipate. Typically, only a few excitation cycles are needed to obtain accurate results. The proposed method involves regularly sampling the structure and then recovering the system response with a sampling rate over the Nyquist-Shannon limit by exploiting the periodicity of the excitation cycle. This is possible by sampling a certain number of excitation cycles and taking different information about the response every cycle. In this chapter, an overview of the fundamental principles of the Smart Aliasing methodology is provided. Section 8.1 explains the mathematical concepts behind the method, while Section 8.2 presents the applied procedure used to implement the method.

8.1 Mathematical explanation

A fundamental assumption behind this method is that the signal to be reconstructed has to be periodic. When a signal is periodic, it is possible to reconstruct it using signal aliasing. As shown in Equation 3.2, if a signal with a frequency f_o is sampled with a sampling frequency $f_s < f_o$, the resulting signal will be characterized by a frequency $f_a = f_o - f_s$. This concept is illustrated in Figure 3.2. An important property of the aliased signal is that its shape is the same as the original signal but scaled along the time axis.

$$\vec{S_a} = \vec{S_o}|_{\bar{t}=\frac{f_o - f_s}{f_a}\bar{t}} \tag{8.1}$$

where $\vec{S_o}$ is the original signal, $\vec{S_a}$ is the aliased signal and $\bar{t}$ is the time vector in which the signals are evaluated. By measuring the aliased signal with a sampling frequency f_s it is feasible to reconstruct one cycle of the original signal. The reconstructed signal can be defined as:

$$\vec{S_{artif}} = \vec{S_a}|_{\bar{t}=\frac{f_a}{f_o-f_s}\bar{t}} \tag{8.2}$$

To achieve the reconstruction of the original signal, the same samples that characterize the aliased signal should be sampled at a frequency $f_r = \frac{f_o}{f_a} f_s$. This frequency corresponds to the sampling frequency f_s scaled by the ratio between original signal frequency and the aliased signal frequency. Figure 8.1 illustrates this process for a simple signal, but it can be extended to more complex signals composed by multiple sine waves.

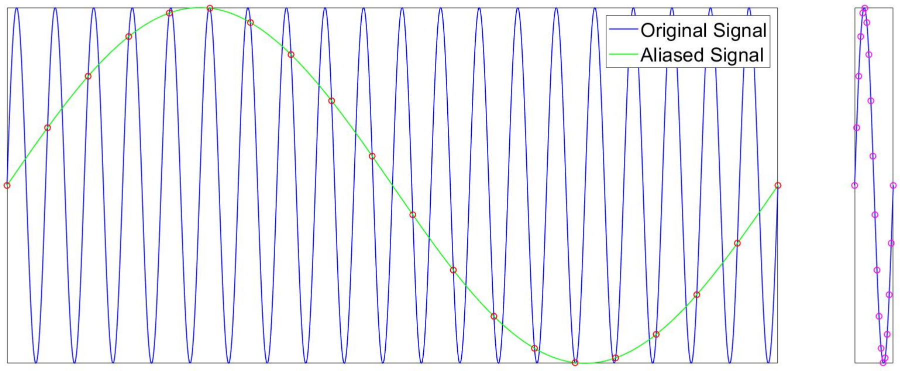

Figure 8.1: Smart Aliasing example

8.2 Experimental procedure

The experimental procedure involves stimulating the system using a pseudo-random signal that excites a specific frequency range. The selection of this particular signal is based on the fact that, when compared to a chirp, the signal's periodicity is more precise. This is because a pseudo-random signal enables the higher frequencies to be continuously excited before the lower frequencies, and vice versa, in order to maintain continuity with the start and end portions of the exciting cycle when it is repeated (see figure 8.2). The selection of the excited frequencies is dependent on the desired frequency range in which natural frequencies are to be identified.

Following a period of non-sampling to allow for the possible transient to end and the attainment of steady-state behaviour, cameras commence sampling the excited structure at a certain sampling frequency f_c, starting from the initial instant of the excitation cycle. At the end of the first cycle, the number of captured images is insufficient for fully describing the behaviour of the structure, since the sampling rate is below the Nyquist-Shannon limit. Let f_s be the final frequency at which

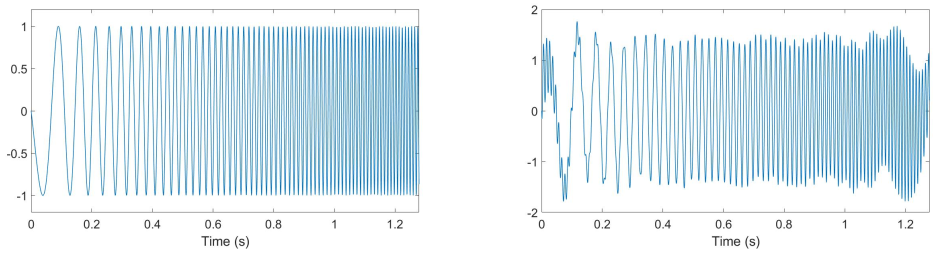

(a) Chirp (b) Psuedorandom

Figure 8.2: Chirp and pseudorandom signals exiting a bandwidth between 5 and 100 Hz

the signal is to be sampled, beyond the Nyquist-Shannon limit. In the subsequent sampled cycle, the cameras begin capturing images at the same frequency f_c, but at a time offset of $1/f_s$ after the initial instant of the excitation cycle. This process is repeated for each subsequent cycle, with the first captured image of each cycle shifted by $1/f_s$ with respect to the previous one. After undergoing $N = f_s/f_c$ cycles of excitation, it becomes possible to obtain a sufficient number of samples to describe the response of the structure, related to a single cycle of excitation, ith a sampling rate of f_s. However, it is necessary to resort the samples appropriately as they were not obtained in chronological order. A limitation of the described procedure is that the ratio between f_s and f_c must be an integer.

Chapter 9

Numerical Validation

This chapter includes a numerical validation of the method to demonstrate its feasibility. Section 9.1 describes the validation procedure and presents the results obtained, while Section 9.2 showcases the results obtained in a particular condition, highlighting an effect observed during the experimental validation.

9.1 Reconstruction method

To validate the described methodology, a three DOF system is analyzed (as shown in Figure 9.1), and its response is under-sampled as described in 8.2 for a certain number of cycles to reconstruct one response cycle. The FRF is then evaluated both from the reconstructed response and the original response of one cycle. The two results are compared to evaluate the capacity of the methods.

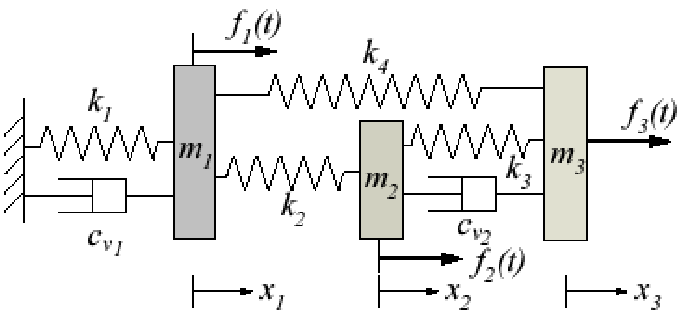

Figure 9.1: Three DOF system anlalyzed for the validation

To simplify the analysis, only one DOF is being excited and its response is being analyzed. Table 9.1 presents the properties of the excitation signal, while the properties of the system are listed in Table 9.2. These system properties were specifically chosen such that the transient response lasted for a certain number of cycles, allowing for the investigation of its effect on the reconstruction method.

Excitation properties	
Excitation signal	Pseudo-rand
Excited DOF	x_3
Bandwidth	5-500 Hz
Sampling freq.	1600 Hz
Spectral lines	1024
Acquistion time	1.28

Table 9.1: Excitation signal properties

System properties	
m_1	$1kg$
m_2	$1kg$
m_3	$1kg$
k_1	$200000N/m$
k_2	$200000N/m$
k_3	$200000N/m$
k_4	$200000N/m$
c_{v1}	$5N/m/s$
c_{v2}	$5N/m/s$

Table 9.2: Three DOF system properties

The camera frame rate, denoted by f_c, and the final sampling frequency, denoted by f_s, are identical to those that will be used during experimental validation, as indicated in Table 9.3.

To carry out the validation process, the system is initially solved to evaluate the response, taking into account the appropriate number of cycles for the excitation. Subsequently, the response is sampled at the camera frame rate, with consideration of time shifting every cycle, and then the samples are sorted to recover the reconstructed single cycle. It is worth noting that the cycles employed to reconstruct the signal began after ten excitation cycles to ensure the transient had ended. Noise is added by taking into account the SNR obtained from experimental pre-tests, resulting in an average of 35 dB throughout the structure.

Smart Aliasing settings	
Camera frequency	25 Hz
Sampling frequency	1600 Hz
N. of averages	2
Excitation cycles needed	64
Delay cylcles	10

Table 9.3: Reconstruction method settings

Figure 9.2 presents a comparison between the reconstructed response cycle and the response of the first cycle used to recover the signal, directly sampled at f_s. The reconstructed cycle is composed of two excitation cycles in order to get two averages of the single cycle when evaluating the reconstructed FRF. The reconstruction process was successful, with a TRAC value of 0.9994 indicating that the reconstructed signal is very similar to the original signal. Additionally, the comparison of the FRFs, shown in Figure 9.3, demonstrates that the modes are well reconstructed.

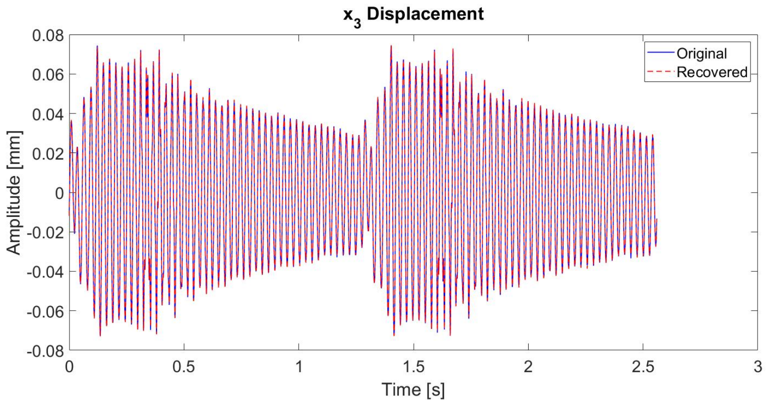

Figure 9.2: Response comparison with 10 delay cycle

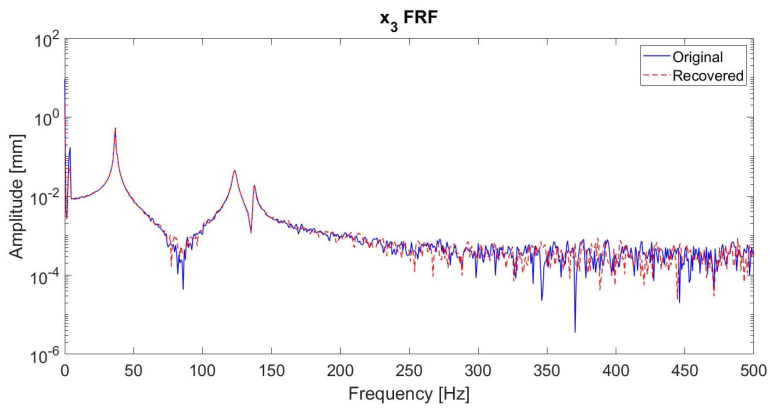

Figure 9.3: FRF comparison with 10 delay cycle

9.2 Transient effect

To assess the impact of the transient on the reconstruction method, and to determine the effects of non-periodic signals, a validation process similar to that described in Section 9.1 is conducted, with the exception that no waiting time was given for the system to reach steady-state behaviour before beginning the sampling process.

In this case, the TRAC value is lower (TRAC = 0.9969), as can be observed in Figure 9.4, which clearly shows that the two time histories are different. Furthermore, in the FRF comparison, it is evident that the recovered FRF is affected by the presence of harmonics that have a periodicity of 25 Hz, which corresponds to the camera frame rate. The fact that the harmonics are caused by the transient is confirmed by plotting the difference between the reference and the reconstructed signals, which reveals the shape of the transient (Figure 9.6). The periodicity of the cycles used to recover the signals with and without waiting for the transient to end is evaluated by calculating the mean of the TRAC values obtained between the mean of all the cycles and each individual cycle. When waiting for the transient to end, this value is 0.9997, while without waiting, it is 0.9085.

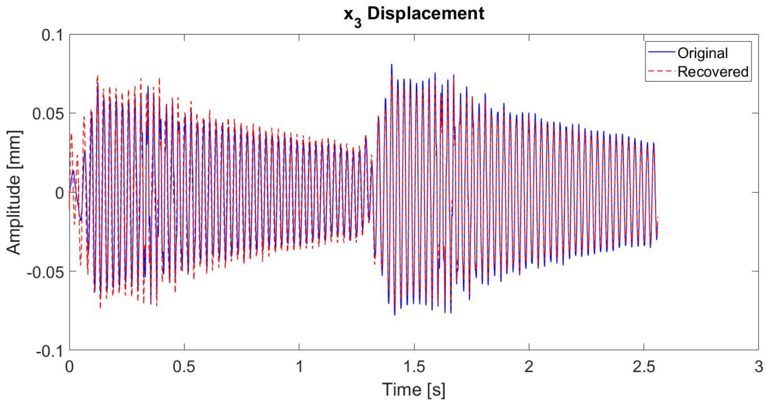

Figure 9.4: Response comparison without delay cycle

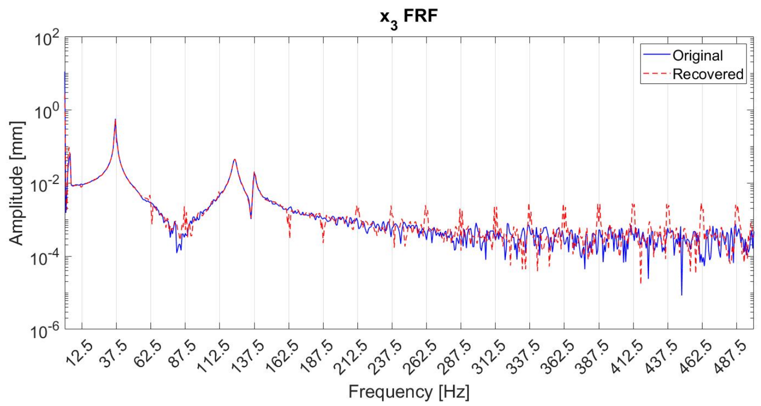

Figure 9.5: FRF comparison without delay cycle

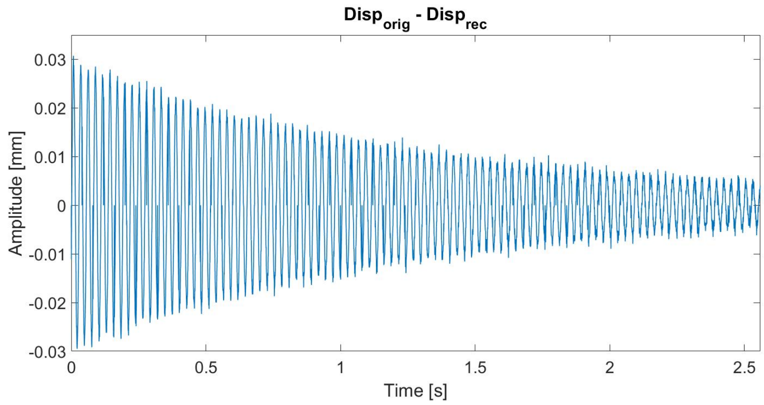

Figure 9.6: Transient effect

Chapter 10

Experimental Validation

Following the numerical validation, the experimental validation is conducted to further validate the Smart Aliasing method through practical tests. This chapter begins with a description of the set-up used in Section 10.1, followed by the presentation of results obtained in Section 10.2. Lastly, in Section 10.3, the results of various tests are compared and further analysis is conducted to explore the presence of harmonics observed in the results.

10.1 Set-up

Figure 10.1 displays all the equipment employed in the experimental validation, which is similar to the one used in the experimental validation conducted for the Random Sampling method (Section 7.2).

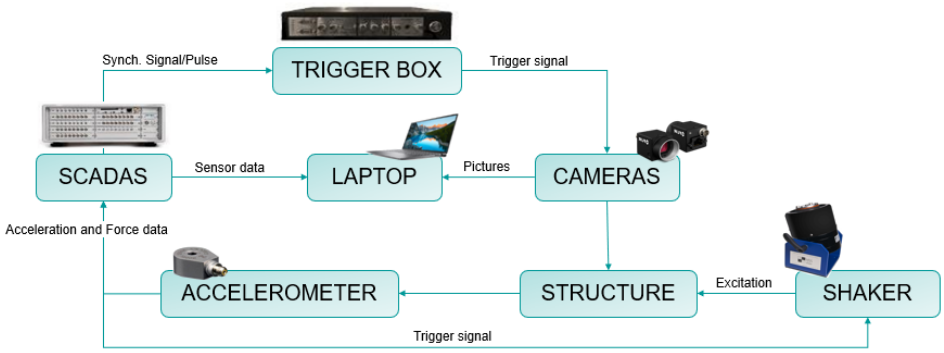

Figure 10.1: Set-up scheme for Smart Aliasing

Given that a periodic excitation is required for this validation, an electrodynamic shaker is used instead of a modal hammer (as shown in Figure 10.2 (b)). The shaker is placed beneath the beam and connected at a location away from a modal node, adjacent to which an uniaxial accelerometer is placed. The shaker is triggered by the SCADAS. To also acquire force data relative to the shaker, a load cell is attached to the end of the rod connecting the shaker to the structure, as depicted in Figure 10.4. The remaining devices in the set-up are the same as those used in the experimental validation for Random Sampling and are connected in a similar manner. It is worth noting that the accelerometer is not used for the same purpose as in the other method, but instead is solely employed to identify frequency peaks and confirm that the natural frequencies obtained through DIC processing are accurate.

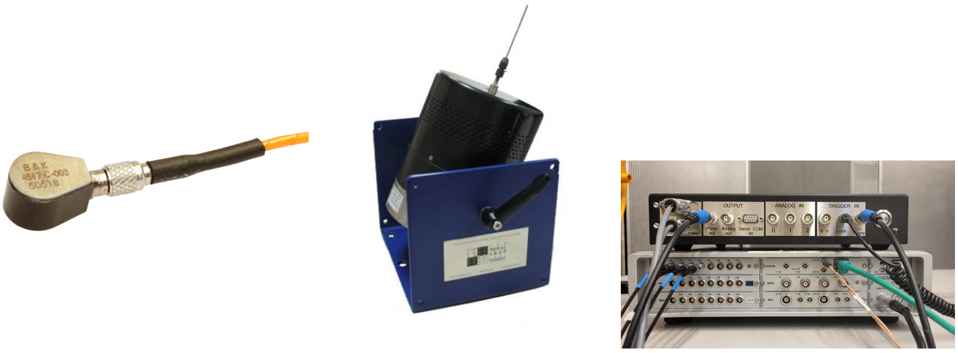

(a) Accelerometer (b) Shaker (c) SCADAS and Triggerbox

Figure 10.2: Used devices

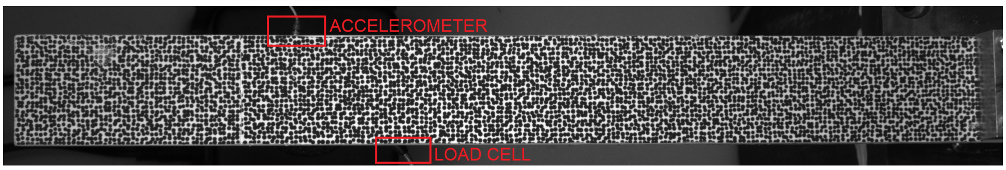

Figure 10.3: Test picture of the beam for Smart Aliasing test

Figure 10.4: Link between shaker, load cell and beam

Figure 10.5: Set-up complete for Smart Aliasing

On the software side, also in this case, pictures and signals are acquired through the Siemens Simcenter Testlab software.

Another significant difference in the experimental setup is the method for triggering the cameras. In this case, the cameras are triggered to obtain a regular sampling. To achieve this, two options are available and both are used to better test the methodology, as explained later in this work. The first option is to transmit a synchronization signal with a sawtooth shape from the SCADAS to the Triggerbox. This signal is aligned with the excitation signal, having the same cycle, to ensure proper synchronization of the cameras with the excitation. The Triggerbox would then handle the regular sampling and the shifting every cycle after setting the appropriate parameters in the acquisition software. The second solution is the same as that used for the Random Sampling method. It involves generating a signal consisting of rectangular pulses that is sent to the Triggerbox by the SCADAS. The Triggerbox would then send this signal to the cameras. In this case, the synchronization between the cameras and the excitation signal is ensured by aligning the trigger signal with the excitation signal at the time of its generation. For this validation, only low-speed cameras are used.

10.2 Results

Table 10.1 presents the test report for both the experimental settings and the DIC post-processing. Table 10.2 displays the parameter used for the first test to evaluate the methodology, including the Smart Aliasing settings and excitation signal properties.

Camera Settings	
Noise std	0.0053 mm
Focal length	25 mm
Object-camera distance	$\sim$ 1 m
N. of images	4096
Pixel to mm	0.15
ROI	2448x388 pixels
Frame rate	25 Hz
Exposure time	500 μs
Stereo angle	18°

DIC Settings	
Subset size	25 pixels
Step size	15 pixels
Correlation	ZNSSD
Interpolation	Local bicubic spline
Shape function	Quadratic

Table 10.1: Smart Aliasing tests report

After the structure has been excited for the desired number of cycles, while the cameras recorded the response, the acquired images are processed using Simcenter Testlab DIC Analysis. By sorting all the samples chronologically, it is feasible to derive the reconstructed displacement cycle, which also comprises two excitation

Test parameters	
Camera frequency	25 Hz
Sampling frequency	1600 Hz
Spectral lines	1024
Acquisition time	1.28 s
N. of averages	2
Delay cycles	5
Bandwidth	15-500 Hz
Force peak value	19 N
Excitation signal	Pseudo-rand

Table 10.2: Smart Aliasing setting and excitation parameters

cycles to determine an average behaviour of the structure. Based on the reconstructed displacement and by knowing the excitation force applied in a single cycle, the FRF sum can be evaluated (see Figure 10.6). Subsequently, the mode shapes can be determined (see Figure 10.7) via Polymax.

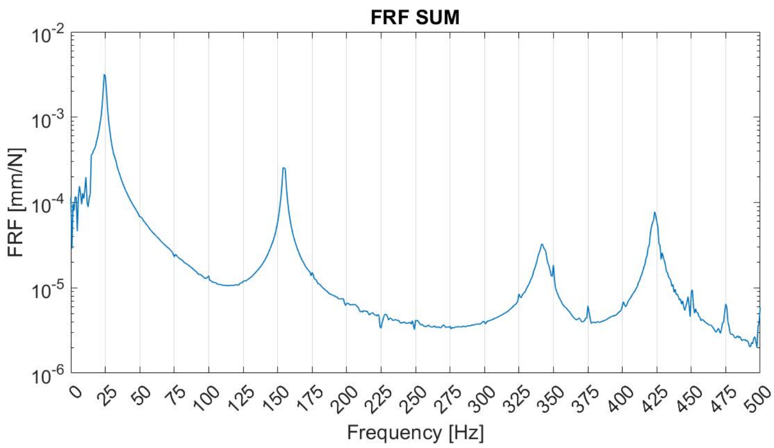

Figure 10.6: FRF obtained with Smart Aliasing reconstruction

The results in terms of FRF sum and mode shapes illustrate the precise reconstruction of the modes, exhibiting all the modes within the excited bandwidth, including the three bending modes and the first torsional mode. Furthermore, a validation check was conducted by comparing the accelerometer data to ensure the precise positioning of the natural frequencies. However, upon examining the grid at 25 Hz intervals, it became apparent that the FRF sum exhibits some harmonics with a periodicity of 25 Hz which are not associated with the structure's behaviour.

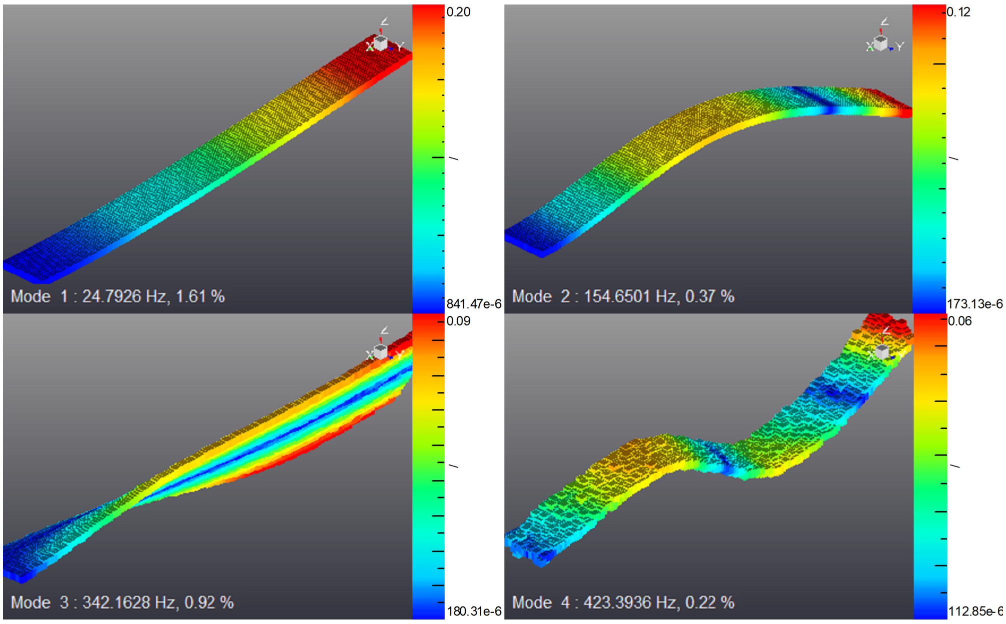

Figure 10.7: Mode shapes obtained with Smart Aliasing reconstruction

10.3 Harmonics investigation

Since this methodology was previously tested in other studies [11], and its primary issue was the presence of harmonics, the subsequent tests were conducted to analyze and investigate the source of these harmonics to enhance the methodology's quality. Various tests were performed to investigate the harmonics by changing certain parameters to comprehend their cause. The camera settings and processing options employed in these tests were consistent with those detailed in Table 10.1.

10.3.1 Periodicity verification

The proposed method is based on the assumption that the signal to be reconstructed is periodic, therefore a periodic excitation is necessary to achieve this. Thus, the first step in investigating the presence of harmonics in the FRF results involves measuring the periodicity of both the excitation signal and the acquired response relative to a test conducted using the proposed methodology. To evaluate the periodicity of the excitation signal, the mean of the TRAC values is calculated between the mean of all the excitation cycles needed to reconstruct the response with every cycle. This resulted in a value equal to 1, indicating that the excitation signal is precisely periodic. Figure 10.8 (a) provides a graphic comparison between two excitation cycles as an example. In order to estimate the periodicity of the recovered response, the TRAC value is calculated between the response relative to the two excitation cycles, as the reconstructed displacement is made up of two excitation cycles in order to consider the average behavior. The TRAC value is calculated to be 0.9995. Figure 10.8 (b) depicts the comparison between the two displacement cycles compared. This indicates that the reconstructed response is mainly periodic, but the small differences between the cycles could be responsible for the presence of harmonics. It should be noted that this is a preliminary analysis, and further investigation is necessary to fully understand the presence of harmonics in the FRF results.

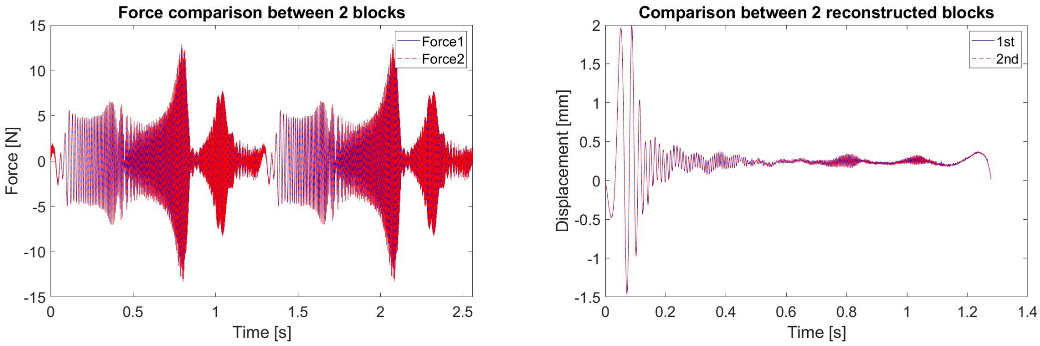

(a) (b)

Figure 10.8: Excitation signal and recovered response periodicity verification

10.3.2 Different excitation force

As a second analysis to investigate the harmonics, a series of tests are conducted by modifying the level of the forcing function applied by the shaker to determine its impact on the results. The initial observation was that the harmonics are less noticeable when the excitation force is increased. Figure 10.9 illustrates the FRF sum of various tests conducted with varying the level of the excitation force. It is evident that the harmonic peaks are more pronounced at lower forcing function level, particularly when examining the plot zoomed in. Generally, when analyzing the modes, a higher force results in a greater displacement, enabling better mode shapes to be obtained due to the increased SNR. Nevertheless, the difference in the height of the harmonic peaks must be linked to a disparity in SNR caused by different displacement levels. This is because the harmonics are produced by an effect similar to the one discussed in Section 9.2, which exhibits a consistent level regardless of the applied force.

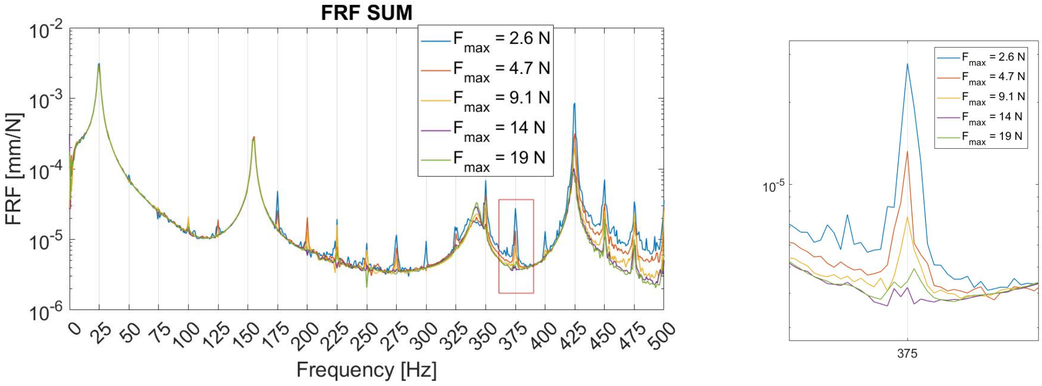

Figure 10.9: FRF sum comparison obtained with different forcing function

10.3.3 Different delay cycles

As mentioned in Section 9.2, when image acquisition begins before the conclusion of the initial transient harmonics are present in the reconstructed FRF. Therefore, experiments are conducted by varying the number of cycles waited before initiating image acquisition. In Figure 10.10, FRF sum obtained from four different tests with varying numbers of delay cycles are shown. In Figure 10.10 (a), two tests with lower forcing functions and different numbers of delay cycles are compared, while in Figure 10.10 (b), the same comparison is made with a higher forcing function. From this comparison, it can be inferred that the initial transient is not the cause of the harmonics, since the height of the harmonic peaks does not change significantly with the number of delay cycles.

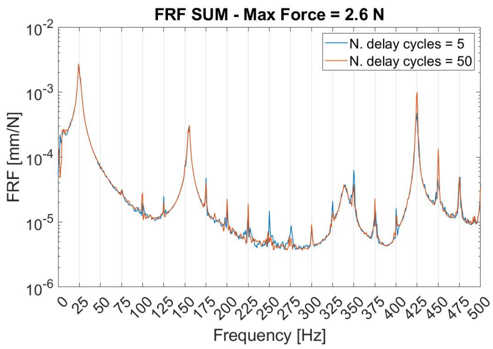

(a) Lower forcing function

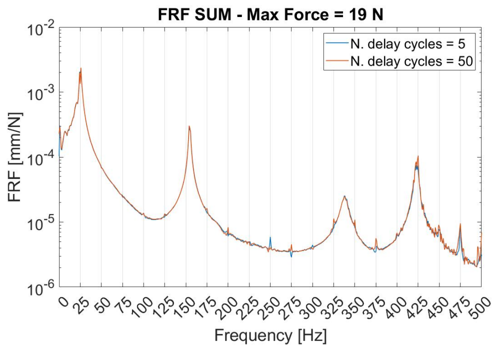

(b) Higher forcing function

Figure 10.10: FRF sum comparison obtained with different delay cylces

10.3.4 Different testing methods

Considering the potential to carry out camera triggering using diverse approaches and the interdependence between harmonics and camera frame rate, it was necessary to verify whether the presence of harmonics was a result of the Smart Aliasing method or the execution of the camera triggering. To accomplish this, three distinct approaches are implemented and compared. These methodologies are detailed and explained as follows:

- **Pulse shifting with Triggerbox** is the method employed to obtain the previously displayed test results. This approach involves transmitting the synchronization signal, which is synchronized with the excitation signal, to the Triggerbox. Upon configuring the camera frame rate, final sampling frequency, and synchronization signal frequency, the Triggerbox captures the image while managing the shifting at the beginning of each cycle.
- **Pulse Shifting with SCADAS** also involves shifting the first pulse during each cycle, similar to the previous method described. However, in this approach, SCADAS directly transmits a rectangular signal to the Triggerbox, where each rectangular pulse corresponds to an image to be captured and subsequently transmitted to the cameras. The rectangular signal is appropriately aligned with the excitation signal during its creation.
- **Force shifting** method also involves sending a rectangular signal to the Triggerbox, similar to the previous method described. However, in this approach, the camera's sampling rate is fixed at 25 Hz without any pulse shifting. Instead, the cycle of the forcing function is made shorter by the same amount of time Δt as the pulse shifting in the previous methods. This is done to ensure that the reconstruction methods function in the same manner.

Figure 10.11 displays a comparison of the three methods used to conduct tests at two different levels of excitation force. It can be observed that the results in terms of FRF sum are approximately identical, and the height of the harmonic peaks is also similar. These findings confirm that the presence of harmonics is a result of the methodology itself and not the implementation of the method.

10.3.5 Comparison between cameras and accelerometer

To further confirm that the presence of harmonics is a result of the reconstruction method and that is not dependent on the cameras, the FRF obtained from accelerometer data is evaluated by reconstructing the acceleration in the same manner as the displacement captured by the cameras. Figure 10.12 presents a comparison of the FRF sum obtained from the displacement reconstructed from

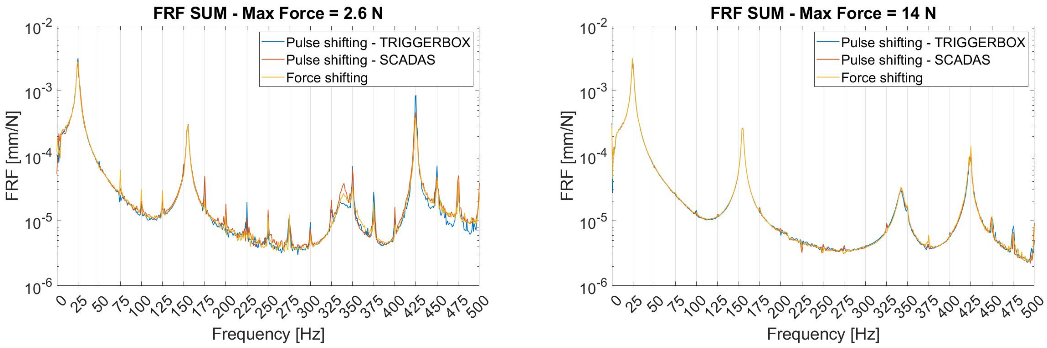

Figure 10.11: FRF sum comparison obtained with different triggering methods

the data acquired by the cameras with the FRF obtained from the acceleration reconstructed from the accelerometer data. Although the harmonics are barely visible in the accelerometer FRF, some peaks can be observed within the red ellipses. This analysis was conducted using a low excitation force in order to obtain a lower SNR and more accurately assess the presence of harmonics. The presence of harmonics in the FRF obtained with the reconstructed accelerometer data confirms the hypothesis. The SNR of the signals used to generate the FRFs was evaluated to determine if the difference in visibility of the harmonic peaks between the acceleration data and the displacement data could be attributed to a difference in SNR. The resulting SNR was approximately 70 dB for the accelerometer data and 40 dB for the displacement. For the displacement, the signal related to the point with the highest displacement was considered.

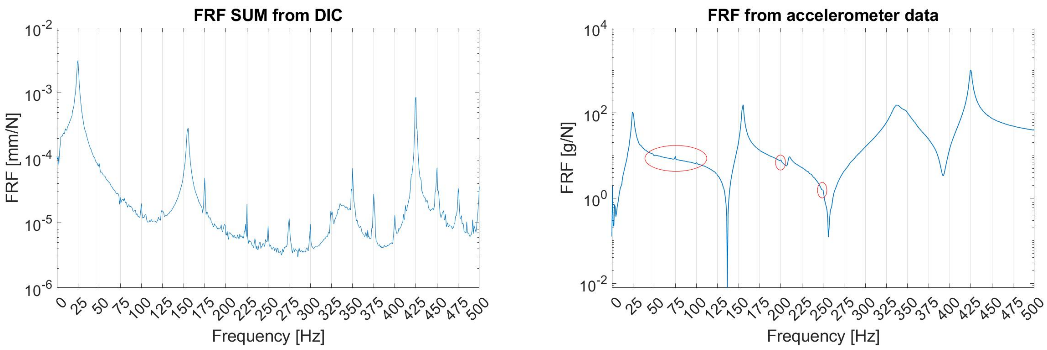

Figure 10.12: FRF comparison between camera and acclerometer data

10.3.6 Noise evaluation

In order to gain a better understanding of the origin of the observed harmonics, two tests are conducted without applying any excitation. In the first test, images of the unexcited beam are captured, while in the second test, images of the surface of the weight used to clamp the beam are captured. In both cases, the surface under analysis is appropriately speckled, and on the same surface is attached an accelerometer. The objective of these two tests was to investigate the noise recorded by the cameras and the accelerometer to determine the source of the harmonics. It is clear from the numerical validation that pure noise does not generate harmonics, while a transient is more likely to be the source of this phenomenon.

The results obtained from testing the beam not excited by the shaker are illustrated in Figure 10.13. Figure 10.13 (a) presents a comparison of the FFT sum derived from the reconstructed displacement with the FFT sum obtained from the displacement sampled at 25 Hz without sorting the images. The comparison is shown at the top, while the two displacements used to evaluate the FFTs are compared at the bottom (Figure 10.13 (c)). The x-axis scale for the non-reconstructed displacement is incorrect and has been compared for simplicity in 2.56 s. Figure 10.13 (b) compares the FFT obtained from the accelerometer data. In this case, only one time history is considered as a single accelerometer is used. The reconstructed FFT is obtained as usual, while the non-reconstructed FFT is derived from the acceleration directly sampled at the final frequency. Upon examining the reconstructed FFTs, it is evident that in both cases, there is some effect that, like a transient, generates harmonics during the reconstruction process. Specifically, when analyzing the acceleration registered without reconstruction, it is observed that there are lower frequency components present in addition to the noise. This component in the reconstructed acceleration generates peaks every 1/25 s. The observed behaviour of the acceleration can be attributed to the fact that the structure is clamped on only one side and, hence, not entirely rigid. Therefore, the noise observed in the accelerometer measurements may not be purely random due to the high sensitivity of the accelerometer. In the case of the displacement, the behaviour that generates the harmonics in the FFT is less clear and requires further investigation, as the cameras are not as sensitive as the accelerometer.

Based on the results of the first test, it was deemed necessary to perform a second test on a rigid structure. Figure 10.14 presents a comparison between acceleration and displacement similar to Figure 10.13. However, in this case, the speckle and the accelerometer were placed on a weight to ensure that only pure noise was being analyzed. The results of the second test reveal that no harmonics are present in the FFT obtained by reconstructing the measured acceleration. However, when reconstructing the cameras' displacement using FFT, harmonics are still visible, as observed in the previous tests. Therefore, the results confirm that the cameras are

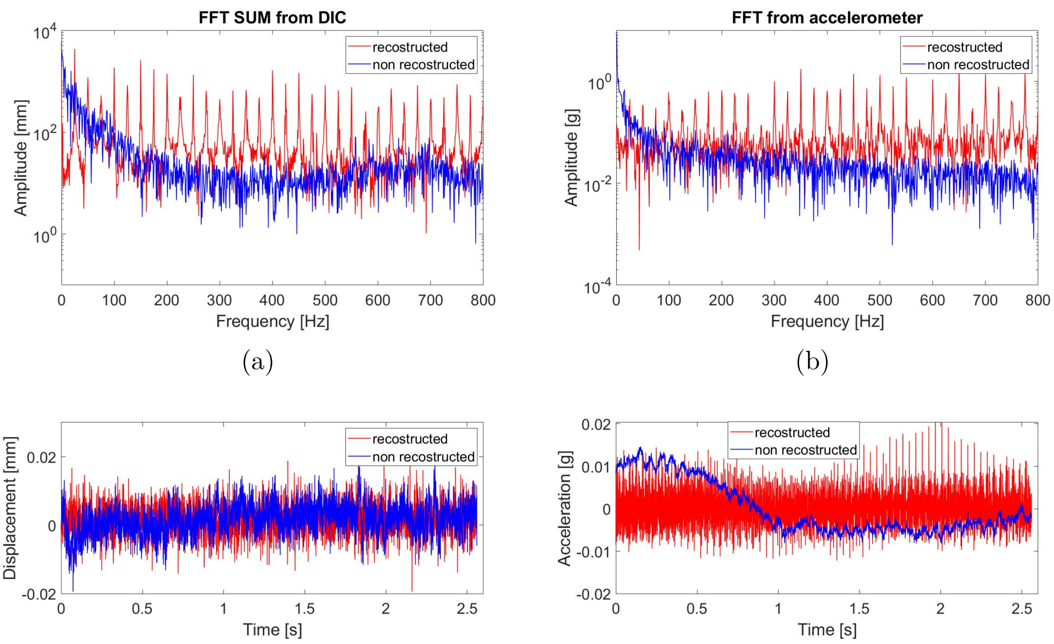

(a) (b)

(c) (d)

Figure 10.13: Results testing the steady beam

unable to capture the same low-frequency behaviour that generates the harmonics observed in the accelerometer data.

In conclusion, the observed harmonics are generated by a behaviour that is not purely random noise. This behaviour is particularly evident in Figure 10.15, which shows the displacement of the beam obtained by triggering the cameras at 25 Hz when it is not excited. The plot includes the mean displacement relative to all points and the displacement relative to one point on the edge. In particular, the low-frequency behaviour is evident in the mean displacement. One possible hypothesis for the source of this behavior is the presence of heat waves generated by the lighting used to illuminate the specimen, which could be contaminating the results. Investigating this possibility could be a future step in this study.

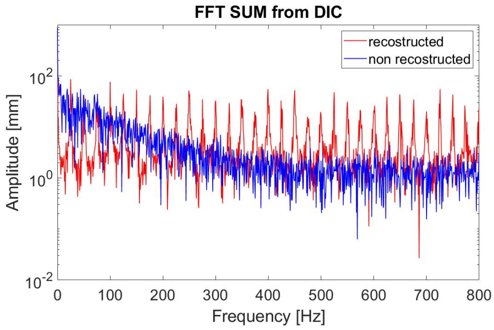

(a)

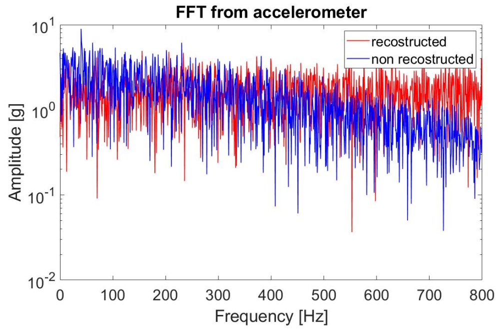

(b)

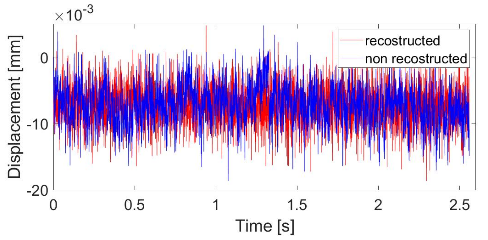

(c)

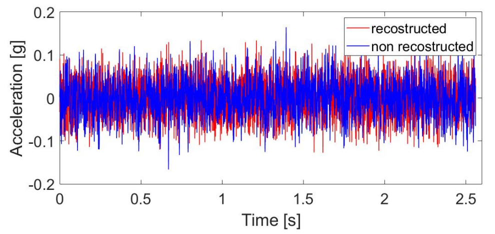

(d)

Figure 10.14: Results testing the steady weight

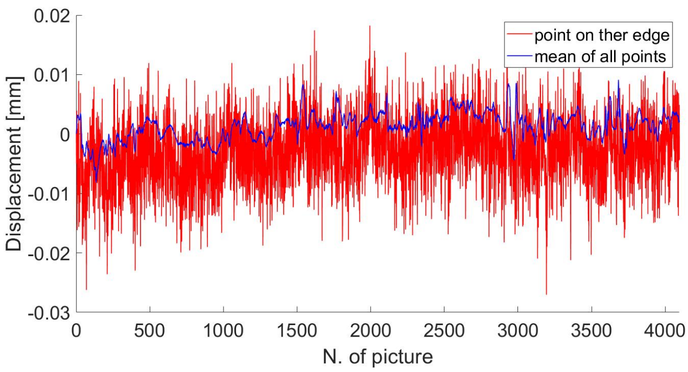

Figure 10.15: Acquired displacement of the unexcited beam

Conclusion and future developments

The present thesis explores two methodologies that aim to extend the frequency characterization capabilities of low-speed cameras beyond the Nyquist-Shannon limit. The effectiveness of both techniques was assessed through a combination of numerical validation, where experimental conditions were replicated in a software environment, and experimental testing, which was performed in a laboratory setting. The first methodology, referred to as Random Sampling, uses nonlinear optimization techniques to reconstruct a high-sampled behavior from a random sparse set of samples, and it is applied in the context of impact testing. The second methodology, known as Smart Aliasing, relies on an acquisition technique that leverages the repetition of an excitation cycle to reconstruct high-sampled behavior from samples acquired with low-speed cameras. The primary aim of both methodologies is to enable structural behavior analysis through the evaluation of modal parameters and mode shapes.

Random Sampling

Based on the findings, the first methodology, Random Sampling, was able to successfully recover the original response in both time and frequency domains during numerical validation using the sparse data. However, the accuracy of the optimization process decreases when the damping is higher, and particularly when SNR decrease. During the experimental testing phase, the optimization process was unable to recover all the mode shapes in the excited bandwidth, particularly the third and fourth modes. However, when the optimization process was applied to a different test dataset, more mode shapes at higher frequencies were successfully reconstructed, highlighting the method's potential. In conclusion, it is clear that the effectiveness of this method depends on the specific test conditions, particularly the damping and level of noise that characterize the response. Therefore, while the method is not currently suitable for the intended purpose, it may serve as a basis for future development. Possible future directions for this research could include improving the optimization algorithm, such as by incorporating force expression into the objective function, or investigating the limits of the methodology more thoroughly, particularly in terms of the impact of damping and noise on the optimization process.

Smart Aliasing

The Smart Aliasing method was able to successfully achieve its intended purpose both in experimental and numerical contexts. The results of the test showed that all mode shapes present in the analyzed bandwidth were accurately reconstructed. Notably, the sampling frequency used to achieve a frequency behavior beyond the Nyquist-Shannon limit was significantly lower than the theoretically required frequency, with a sampling frequency of 25 Hz enabling analysis up to 500 Hz. Although the analyzed frequency can be increased, maintaining the same sampling frequency requires a greater number of repetition cycles, which in turn increases the test duration. Furthermore, the accuracy of the reconstructed data is limited by the presence of harmonics in the reconstructed FRF and the requirement for precise and sufficiently strong periodic excitation to effectively excite the modes is another limitation of the method. It is therefore concluded that this method can be applied for the intended purpose, but with the limitations stated. Future developments related to the Smart Aliasing method can include analyzing the accuracy of estimated modal parameters. To reduce the presence of harmonics, which are more visible at higher frequencies due to a lower displacement, a possible solution is to generate a forcing function that increases when higher frequencies are excited. In addition, a statistical evaluation can be performed to further demonstrate that the harmonics are due to the presence of a low frequency component in the background noise and further analysis can be conducted to determine the source of the harmonics. For instance, it is possible that the harmonics are generated by heat waves resulting from the warm environment produced by the lights.

In conclusion, this study represents a significant advancement in the analysis of this methodologies and demonstrates the potential benefits of using low-speed cameras for EMA, which can substantially reduce testing costs and the image resolution compared to high-speed cameras.

Bibliography

[1] Alessandro Zanarini. «Full field optical measurements in experimental modal analysis and model updating». In: *Journal of Sound and Vibration* 442 (2019). ISSN: 10958568. DOI: 10.1016/j.jsv.2018.09.048 (cit. on p. 1).

[2] Javad Baqersad, Peyman Poozesh, Christopher Niezrecki, and Peter Avitabile. «Photogrammetry and optical methods in structural dynamics – A review». In: *Mechanical Systems and Signal Processing* 86 (2017). ISSN: 10961216. DOI: 10.1016/j.ymssp.2016.02.011 (cit. on p. 1).

[3] Dionysius M. Siringoringo and Yozo Fujino. «Noncontact operational modal analysis of structural members by laser doppler vibrometer». In: *Computer-Aided Civil and Infrastructure Engineering* 24 (4 2009). ISSN: 10939687. DOI: 10.1111/j.1467-8667.2008.00585.x (cit. on p. 1).

[4] E. Di Lorenzo, P. Lava, R. Balcaen, S. Manzato, and B. Peeters. «Full-field modal analysis using high-speed 3D digital image correlation». In: vol. 1149. 2018. DOI: 10.1088/1742-6596/1149/1/012007 (cit. on p. 1).

[5] Javad Baqersad, Jennifer Carr, Troy Lundstrom, Christopher Niezrecki, Peter Avitabile, and Micheal Slattery. «Dynamic characteristics of a wind turbine blade using 3D digital image correlation». In: vol. 8348. 2012. DOI: 10.1117/12.915377 (cit. on p. 2).

[6] Ahmed Yashar, Neil Ferguson, and Maryam Ghandchi Tehrani. «Measurement of rotating beam vibration using optical (DIC) techniques». In: vol. 199. 2017. DOI: 10.1016/j.proeng.2017.09.052 (cit. on p. 2).

[7] Tomaž Bregar, Klemen Zaletelj, Gregor Čepon, Janko Slavič, and Miha Boltežar. «Full-field FRF estimation from noisy high-speed-camera data using a dynamic substructuring approach». In: *Mechanical Systems and Signal Processing* 150 (2021). ISSN: 10961216. DOI: 10.1016/j.ymssp.2020.107263 (cit. on p. 2).

[8] Sandro Barone, Paolo Neri, Alessandro Paoli, and Armando Razionale. «Digital Image Correlation Based on Projected Pattern for High Frequency Vibration Measurements». In: *Procedia Manufacturing* 11 (2017). ISSN: 23519789. DOI: 10.1016/j.promfg.2017.07.304 (cit. on p. 2).

[9] Yihao Liu, Hongjian Gao, James Zhuge, and Jeff Zhao. «Research of undersampling technique for digital image correlation in vibration measurement». In: vol. 9B. 2017. DOI: 10.1007/978-3-319-54735-0_6 (cit. on p. 2).

[10] Yonggang Wang, Felix Simeon Egner, Thijs Willems, Matteo Kirchner, and Wim Desmet. «Camera-based experimental modal analysis with impact excitation: Reaching high frequencies thanks to one accelerometer and random sampling in time». In: *Mechanical Systems and Signal Processing* 170 (2022). ISSN: 10961216. DOI: 10.1016/j.ymssp.2022.108879 (cit. on pp. 2, 3, 52).

[11] D. Mastrodicasa, E. Di Lorenzo, B. Peeters, and P. Guillaume. «A demo airplane full field modal validation using digital image correlation». In: 2020 (cit. on pp. 2, 3, 69).

[12] Jae Young Park, Michael B. Wakin, and Anna C. Gilbert. «Modal analysis with compressive measurements». In: *IEEE Transactions on Signal Processing* 62 (7 2014). ISSN: 1053587X. DOI: 10.1109/TSP.2014.2302736 (cit. on p. 3).

[13] Zai Yang and Lihua Xie. «Exact Joint Sparse Frequency Recovery via Optimization Methods». In: vol. 64. 2016. DOI: 10.1109/TSP.2016.2576422 (cit. on p. 3).

[14] Ward Heylen, Stefan Lemmens, and Paul Sas. *Modal Analysis Theory and Testing*. 1997 (cit. on pp. 5, 13, 17).

[15] Peter Avitabile. «Experimental modal analysis a simple non-mathematical presentation». In: *S V Sound and Vibration* 35 (1 2001). ISSN: 00381810 (cit. on pp. 5, 17).

[16] Bart Peeters, Herman Van Der Auweraer, Patrick Guillaume, and Jan Leuridan. «The PolyMAX frequency-domain method: A new standard for modal parameter estimation?» In: *Shock and Vibration* 11 (3-4 2004). ISSN: 10709622. DOI: 10.1155/2004/523692 (cit. on p. 13).

[17] Chunli Wu, Hanbing Liu, Xuxi Qin, and Jing Wang. «Stabilization diagrams to distinguish physical modes and spurious modes for structural parameter identification». In: *Journal of Vibroengineering* 19 (4 2017). ISSN: 13928716. DOI: 10.21595/jve.2017.17629 (cit. on p. 14).

[18] Nick McCormick and Jerry Lord. «Digital imagine correlation». In: *Materials Today* (2010). ISSN: 13697021. DOI: 10.1016/S1369-7021(10)70235-2 (cit. on p. 22).

[19] Elizabeth M C Jones et al. «A Good Practices Guide for Digital Image Correlation». In: *International Digital Image Correlation Society* (2018) (cit. on pp. 24, 25).

[20] Jorge J. Moré and D. C. Sorensen. «Computing a Trust Region Step». In: *SIAM Journal on Scientific and Statistical Computing* 4 (3 1983). ISSN: 0196-5204. DOI: 10.1137/0904038 (cit. on p. 30).